Bernardo Matos Alves Costa Ferreira

Licenciado em Engenharia Micro e Nanotecnologia

Glass Microfluidic platforms for molecular detection by SERS

Dissertação para Obtenção do Grau de Mestre em

Engenharia Micro e Nanotecnologias

Orientador: Prof. Doutor Hugo Manuel Brito Águas, Faculdade de Ciências e Tecnologia da Universidade Nova de Lisboa

Co-orientadores: Doutora Ana Cláudia Madeira Botas Gomes Pimentel, Faculdade de Ciências e Tecnologia da Universidade Nova de Lisboa

Prof. Doutor José Ricardo Franco Tavares, Faculdade de Ciências e Tecnologia da Universidade Nova de Lisboa

Júri

Presidente: Prof. Doutor Rodrigo Martins

Arguente: Doutor César Laia

Vogais: Prof. Doutor Hugo Águas

FACULDADE DE CIÊNCIAS E TECNOLOGIA
UNIVERSIDADE NOVA DE LISBOA

Glass Microfluidic platforms for molecular detection by SERS

Two roads diverged in a yellow wood,
And sorry I could not travel both
And be one traveller, long I stood
And looked down one as far as I could
To where it bent in the undergrowth;

Then took the other, as just as fair,
And having perhaps the better claim,
Because it was grassy and wanted wear;
Though as for that the passing there
Had worn them really about the same,

And both that morning equally lay
In leaves no step had trodden black.
Oh, I kept the first for another day!
Yet knowing how way leads on to way,
I doubted if I should ever come back.

I shall be telling this with a sigh
Somewhere ages and ages hence:
Two roads diverged in a wood, and I—
I took the one less traveled by,
And that has made all the difference.

Robert Frost

Acknowledgements

No final desta longa e importante etapa na minha vida, queria agradecer a todos que de uma forma ou outra me acompanharam, me ajudaram e tornaram este momento possível. Deste modo quero começar por agradecer à Faculdade de Ciências e Tecnologias da Universidade de Lisboa, e ao departamento de Ciências dos Materias por me terem acolhido tão bem durante estes anos neste grande curso de Micro e Nanotecnologias. Por isso, agradeço também, ao Prof. Dr. Rodrigo Martins e à Prof. Dra, Elvira Fortunato por terem criado este curso e dado todas as ferramentas necessárias e não só, para a formação de engenheiros com espirito crítico, prática laboratorial e bases que poucos ou nenhum outro curso têm. Queria também agradecer ao departamento de conservação e restauro por disponibilizarem o Raman.

De seguida gostaria de agradecer ao meu orientador Hugo Águas por me ter aceitado neste projecto e acompanhado durante todo o processo com a partilha de conhecimentos, ideias e sempre disponível. À minha coorientadora Dra. Ana Pimentel, por me ter ajudado na síntese de nanorods e partilhado ideias que me ajudaram em várias situações. Ao meu coorientador Professor Ricardo Franco pelos conselhos, ajuda e encorajamento ao longo do projecto. À Mestre Andreia Araújo por todo o tempo disponibilizado, pelas várias deposições na câmara limpa, e todas as ideias, conhecimentos e orientações ao longo do projeto. À Mestre Maria João, por toda a paciência, ajuda no Raman, encorajamento, constante disponibilidade, por me guiar e apoiar em todo este percurso. À Daniela Gomes pelas magníficas imagens SEM, sem elas a tese não seria a mesma coisa. À Alexandra Gonçalves e à Sónia Pereira pela paciência, ajuda, disponibilidade e boa disposição. À Ana Carolina pela ajuda no laser. Ao Pedro Alves pela ajuda no PDMS. A todos os colegas, amigos que me acompanharam neste percurso. Obrigado Paul, Jaime, Rodrigo, Anas, Andreia, Rosa, Tomás, Iris, Bruno, Emanuel, Gonçalo, Almeida, Gabi.

A todos os meus amigos, que me têm acompanhado sempre, desde sempre. Tocha e Vítor, especialmente, por todos estes anos a aturar-me, um Obrigado. Aos meus grandes amigos Flores, um irmão para mim, Nandes, César e Braga, tamos cá! Sem vocês não seria a mesma coisa.

Finalmente, à minha família. Especialmente à minha mãe que esteve sempre presente e me ajudou sempre, não há palavras suficientes para agradecer, sou um sortudo. À Sofia, estarei sempre presente quando for preciso e sabes que gosto muito de ti. Ao António pelo o apoio constante e pela ajuda na tese. Ao meu Pai, por todo o apoio, força e

motivação. Aos meus avós por todo o seu apoio, carinho, força e todos os bons momentos.
To Jana, thank you for all the patience, all this moments.

Há sem dúvida quem ame o infinito,
Há sem dúvida quem deseje o impossível,
Há sem dúvida quem não queira nada
-
Três tipos de idealistas, e eu nenhum deles:
Porque eu amo infinitamente o finito,
Porque eu desejo impossivelmente o possível,
Porque eu quero tudo, ou um pouco mais, se puder ser,
Ou até se não puder ser...

Fernando Pessoa

Resumo

Atualmente têm sido desenvolvidas tecnologias para a deteção de contaminantes alimentares face à crescente preocupação na saúde pública. Todavia, os métodos hoje existentes são morosos, dispendiosos e complexos para serem aplicados na indústria alimentar. Assim, o presente trabalho tem como objetivo o desenvolvimento de um dispositivo de microfluídica viável para o uso da espectroscopia de Raman aumentada pela superfície (SERS).

A SERS consiste numa técnica simples, robusta, sensível e rápida para a deteção de componentes vestigiais, podem ser vantajosamente aplicada à deteção de contaminantes alimentares. Foi realizado um estudo dos vários parâmetros de síntese hidrotermal assistido por microondas para crescimento de nanorods de óxido de zinco (temperatura, o tempo e pH). Posteriormente, os nanorods de óxido de zinco foram revestidos por nanopartículas de prata (espessuras de 2, 4, 6 e 8 nm), formadas por deposição física de vapor (PVD) de prata, originando o substrato SERS, AgNP@ZnO*NR*. A eficiência dos vários substratos produzidos foi semelhante independentemente da espessura de prata aplicada, observando-se valores de *enhancement factor* (EF) de SERS entre ~10^5- ~10^6. Paralelamente foram desenvolvidos nanorods em forma de obeliscos tendo resultado numa boa eficiência em SERS, apresentando EF~10^6.

Finalmente, foi criado um dispositivo de microfluídica em PDMS o qual permitiu conduzir uma solução de rodamina-6G sendo observado o seu sinal de SERS no interior do dispositivo. Os ensaios desenvolvidos no decorrer da presente dissertação permitiram inferir sobre o comportamento do sinal de SERS em relação aos parâmetros geométricos dos componentes do substrato para SERS.

Palavras-chave: microfluídica, espectroscopia de Raman aumentada pela superfície, óxido de zinco; nanorods.

Abstract

Nowadays due to increasing concerns in public health, technologies have been developed for the sensitive detection of food contaminants. Since current methods are time-consuming, expensive and complex to operate, this project has as the objective to develop a microfluidics device for surface enhanced Raman spectroscopy (SERS).

SERS consists in a simple, robust, sensitive and fast technique for detection of vestigial components that can be advantageously adapted to the detection of food contaminants. In order to develop an appropriate substrate for SERS, a study was performed of different parameters for the hydrothermal synthesis of zinc oxide nanorods (temperature, time and pH). Afterwards, they were covered with silver nanoparticles with different thicknesses (2, 4, 6 e 8 nm) deposited by physical vapour deposition (PVD), originating the substrate *Ag NPs*@ZnONRs. The efficiency of the different substrates was similar, regardless the thickness of silver, with enhancement factor (EF) values around 10^5~10^6. Simultaneously, obelisk nanorods were developed with good SERS efficiency, and EFs around 10^6.

Finally, it was created a microfluidics device in PDMS, which allowed to observe the SERS signal of a rhodamine-6G solution in its interior. The assays performed in the work allowed to infer the behaviour of SERS signal with different geometric parameters of components of SERS substrates.

Keywords: Microfluidics; Surface enhanced Raman spectroscopy (SERS); Zinc oxide (ZnO); nanorods.

Contents

Index of Tables

Index of figures

CHAPTER 5 – ATTACHMENTS

Abbreviations

Absp	Absorptance
AgNP	Silver nanoparticle
CE	Chemical enhancement
CO_2	Carbon dioxide
EF	Enhancement Factor
EM	Electromagnetic enhancement
FWHM	Full width at half maximum
GC	Gas chromatography
HeNe	Helium-neon laser
HPLC	High-performance liquid chromatography
LAFED	Laser assisted flow deposition
LSPR	Localized surface plasmon resonance
NP	Nanoparticle
NRs	Nanorods
PDMS	Polydimethylsiloxane
PVD	Physical vapour deposition
R_{tot}	Total reflectance
R6G	Rhodamine 6G
SEM	Scanning electron microscopy
SEM-FIB	Scanning electron microscopy-Focused ion beam
SERS	Surface-enhanced Raman spectroscopy
UV-Vis	Ultraviolet-Visible
UVO	Ultraviolet-Ozone
T_{tot}	Total transmitance
XRD	X-Ray Diffraction
ZnO	Zinc oxide

Symbols

Au	Gold
Ag	Silver
C	Carbon
C_{RAMAN}	Raman concentration
C_{SERS}	SERS concentration
CH_2	Methylene
I_{RAMAN}	Raman intensity
I_{SERS}	SERS intensity
M	Molar
Min	Minute
nm	Nanometers
µL	Microliter
ºC	Celsius degrees

Motivation and objectives

Nowadays despite extensive methods to protect public health, disease outbreaks from harmful chemicals and microbial threats still occur. Although the continuous advances in chemical analysis such as gas chromatography (GC)[1] and high-performance liquid chromatography (HPLC)[2] led to significant improvements in automation, measurement time, sensitivity and accuracy, they still suffer certain disadvantages, such as the need of trained personnel, complex and time-consuming sample preparation.

As an alternative, a promising technique is the surface-enhanced Raman spectroscopy (SERS). SERS allows to screen single or multiple contaminant classes simultaneously, is simple, fast, inexpensive and a reliable method.[3]

Zinc oxide was chosen as the platform for the SERS structures for its electrical properties, low price and excellent performance in supporting SERS substrates. ZnO provides the possibility to create nanostructures, which, when coupled with Ag, can generate higher detection sensitivity and thus stronger signal enhancements.

Microwave-assisted synthesis has fast reaction time (compared to conventional method such has furnace), less thermal losses and allows the control of kinetic conditions (time, temperature and pressure), making it a very interesting and promising technique for the development of zinc nanostructures.

Thermal evaporation assisted by electron beam was used to obtain silver nanoparticles (AgNP). This process promotes a good homogeneity and stability, by forming self-assembled NPs.

For its precise control and ability to create a lab-on-a-chip, microfluidics devices offer great advantages for SERS platforms towards point of need applications.

The objective of the present work, considering the techniques previously mentioned, is to develop an efficient SERS microfluidics device, using ZnO nanorods (ZnO NRs) with Ag nanoparticles (Ag NPs) or thin films (Figure 1) to be applied in microfluidic devices.

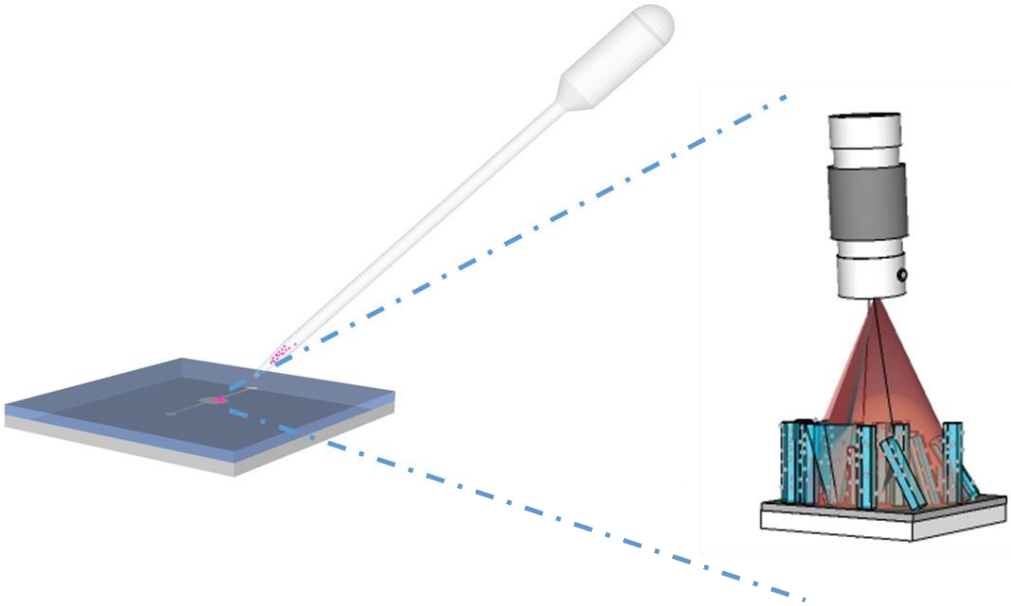

Figure 1 - Schematics of a microfluidic device incorporating a SERS substrate.

1 Introduction

1.1 Surface-Enhanced Raman Spectroscopy

In early 20th century two vibrational spectroscopy methods appeared infrared (IR) and Raman via two different mechanisms: the direct absorption of photons (IR) and the inelastic scattering of photons (Raman). These molecular vibrations were unique for every given molecular structure. Raman spectroscopy has been less used than IR due to its relative weak signals, fluorescence interference and high cost of equipment. As an advantage in relation to IR spectroscopy, especially for biological systems, Raman has less interference from water signals.[4,5]

Raman spectroscopy relies on the inelastic scattering of a photon from a molecule where the frequency changes precisely matching the difference in vibrational energy levels (Figure 1.1).[5]

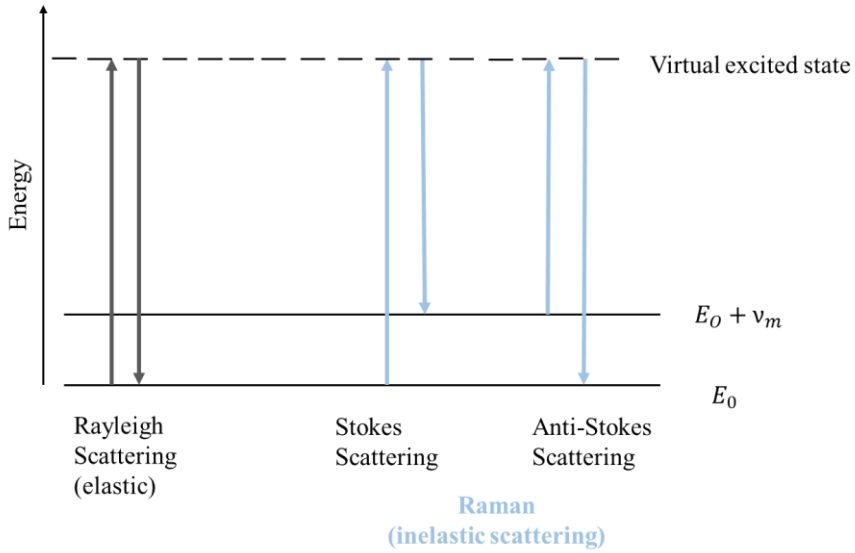

Figure 1.1 - Energy diagram representing (from left to right) the elastic Rayleigh scattering and the inelastic Stokes (*left*) and Stokes (*right*) Raman scattering (*adapted from*[4,5]).

In 1974 it was found that weak Raman scattering signals can be greatly enhanced using noble metal nanostructures (Figure 1.2).[6,7]

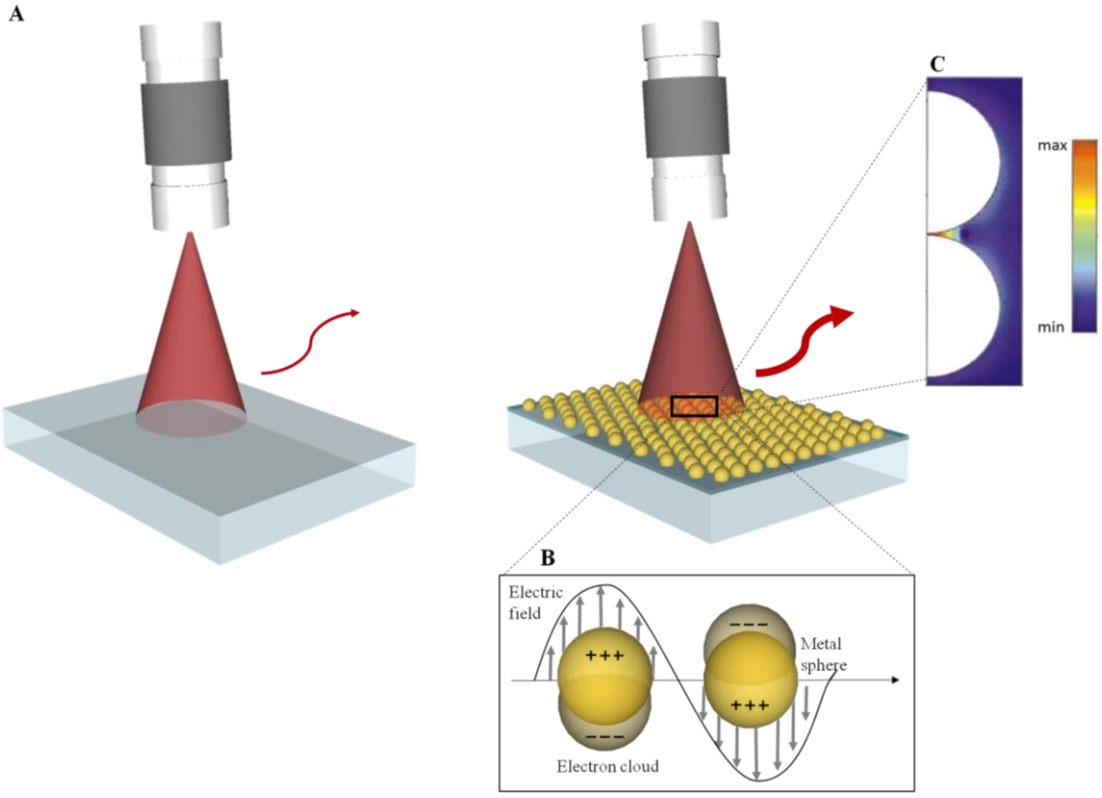

Figure 1.2 – A) Schematic representation of Raman analysis (*right* side) and SERS with metal NPs (*left* side); B) Illustration of LSPR effect; C) Electromagnetic enhancement for dimer configurations of two spheres.

1.1.1 Electromagnetic enhancement effect

The electromagnetic enhancement (EM) is due to the interaction of an electromagnetic wave with a metal surface. The electromagnetic wave, with a specific angular frequency, excites resonantly the delocalized conduction electrons in a metal (*plasmons*), resulting in an amplification of the electromagnetic fields near the surface.[4,8,9]

When the valence electrons of the metal nanoparticle are in a collective oscillation with the frequency of the incident light, occurs the LSPR (Figure 1.2).[4,10]

1.1.2 Chemical enhancement

The chemical enhancement mechanism is generated by the direct interaction of adsorbed molecules with the metal surface, which results in a charge transfer, leading to changes in the polarizability and vibrational modes. The polarizability of the molecule is changed by the charge transfer between the molecule in its electronic ground state and

the metal, resulting in a change of the Raman scattering cross-section of the molecule. This changes lead to enhancements in the range of one to three order of magnitude for Raman scattering, significantly smaller than EM.[4,11]

1.2 General concepts of SERS

The most common SERS active substrates are gold (Au) and silver (Ag) colloids with diameters between 10 and 200 nm. The utilization of colloidal nanoparticle solution presents an advantage as a SERS substrate because it minimizes the burning of samples due to heat dissipation through water, allowing the use of high laser power to enhance the Raman signal. Moreover, the presence of large numbers of nanoparticles allows the acquisition of a stable average-spectrum. However, one drawback associated with liquid colloidal nanosubstrates is the required nanoparticle aggregation, where an uncontrolled exaggerated nanoparticles clump may happen, leading to a loss of LSPR.[3,12]

Comparing Ag and Au, Ag presents a higher enhancement due to being more plasmonically active in visible and near IR regions, but Ag is air sensitive while gold is more chemically stable and able to be conjugated with biomolecules.[9,13,14]

SERS enhancement depends highly on the substrates designs, LSPR can be modulated using a variety or parameters as shape, dimension, interparticle gap and environmental surroundings. Thus, the possibilities for manufacturing SERS active surfaces innovative techniques are vast, as nanolithography[15], self-assembly techniques[16] and chemical synthesis of colloidal metal nanoparticles[17].

1.2.1 SERS enhancement factor and *hot spots*

SERS enhancement factor (EF) quantifies the overall Raman signal enhancement by comparing the average SERS signal for the adsorbed molecule on a metal surface, normalized with the normal Raman signal of the same molecule in solution. The average SERS EF can be calculated using the following equation[18]:

$$EF = \frac{I_{SERS}}{I_{RAMAN}} \times \frac{C_{RAMAN}}{C_{SERS}} \qquad (1.1)$$

Where I_{SERS} and I_{RAMAN} are the intensities of a particular vibrational band in an analyte spectrum (in this project: 1360 and 1509 cm^{-1} for R6G), for SERS and normal Raman spectra respectively; while C_{RAMAN} is the concentration that produces Raman signal, and C_{SERS} the concentration of adsorbed molecules in the scattering volume of the

metallic nanostructure.[12] In some literature this formula can be reported as analytical enhancement factor (AEF).

Raman signal enhancements as high as 10^{14} can occur in *hot spots* on SERS substrate due to the combined electromagnetic (EM), chemical enhancement (CE) and resonance signal enhancement mechanisms.[9,13] The *hot spots* are localized between adjacent nanoparticles (< 10 nm) (near-field regions), (Figure 1.2 C) responsible for the global SERS effect. Hence, SERS is a highly distance-dependant phenomenon and the shape and structure of the nanostructures affect significantly the enhancement. A very close gap between the nanoparticles is therefore beneficial for the creation of extremely strong localized electric fields enhancements.[19,20]

1.3 ZnO structures

Zinc oxide (ZnO) nanostructures have been the subject of intensive studies due to their remarkable chemical and physical properties. ZnO is a n-type semiconductor with a wide and direct band gap of 3.3 eV. ZnO physical and chemical properties depend on size, shape, morphology, and crystallinity of the synthesized nanostructures.[21–23]

Several chemical, electrochemical and physical techniques have been used to grow ZnO nanostructures with different morphologies, as such electrodeposition[23,24], electrospinning[25,26], laser assisted flow deposition (LAFED)[27] and hydrothermal synthesis[28], whether by conventional heating or by microwave radiation.[23,29]

1.3.1 Microwave-assisted synthesis

This technique provides the opportunity to complete reactions, by using different power, in shorter times (minutes), since microwaves are able to transfer directly the energy to the reactive species (molecular heating), promoting reactions and transformations that are difficult and require a longer time in conventional heating.[23,29]

In microwave synthesis, heat is generated internally within the materials, so the surface of the materials are cooler than the interior, resulting in a decrease of thermal losses. In addition to the production methods, the kinetic conditions of the primary solution such as pH, temperature and organic additives, play an important role in reaching the desired morphologies.[16,17]

1.4 Microfluidics device

Microfluidics is becoming highly attractive in bioanalysis for its precise control and manipulation of biological samples. Its small size allows the creation of portable lab-on-a-chip devices that facilitate the low detection limits required in biological target identification. Small devices result in faster reaction times, better temperature control, low energy consumption, parallelisation and portability.[30]

Although SERS is a highly specific and sensitive analytical technique it is challenging to obtain repeatable and reproducible results under complex experimental conditions. Those problems can be overcomed using a microfluidic channel, for a more regular geometry and minimizing the damage to the biological analytes, the recording time and the sample volumes.[31]

Microfluidic devices are commonly made from polydimethylsiloxane (PDMS) and other polymers. They can be manufactured by moulding techniques, such as photolithography and soft lithography which are cheap and suitable for the mass scale production. PDMS is biocompatible, thermally stable up to 150 ºC, has the ability to replicate features with approximately 1 nm resolution and excellent optical properties. PDMS can be sealed reversibly onto substrates by conformal contact due to its elasticity by plasma or UVO treatment. For this reasons PDMS was the chosen material for the present work.[7]

Therefore, using the advantages of a precise control and lab-on-a-chip possibilities with microfluidics, combined with the advantages of ZnO nanostructures with Ag NP, this present work aims to develop efficient SERS substrates to be applied in microfluidics devices for molecular detection of food contaminants.

2 Materials and Methods

In this section, an experimental description is made of the synthesis of the ZnO nanorods and the subsequent deposition of AgNPs techniques by PVD. The substrates fabricated were then tested for SERS efficiency.

2.1 Deposition of the ZnO seed layer

The first step for the fabrication of the Ag NP@ZnO NRs is the deposition of a single layer of ZnO seed on a glass substrate by sputtering at room temperature. A ceramic oxide target with a purity of 99 % has been used for the deposition with the following conditions: power density P = 8.2 Wcm^{-2}, distance between the target and substrate, d = 15 cm, deposition pressure, pd = 4×10^{-3} mbar. Prior to the depositions, the chamber was evacuated, using a turbo-molecular pump, to 10^{-6} mbar. For each seed layer thickness it was used different deposition times: 1 h for 100 nm; 1 h 30 min for 150 nm; 2 h for 200 nm and 3 h for 300 nm.

2.2 Synthesis of ZnO Nanostructures

The ZnO NRs have been synthesized with an aqueous solution of 25 mM zinc nitrate hexahydrate ($Zn(NO_3)2{\cdot}6H_2O$; 98 %, CAS:10196-18-6) and 25 mM hexamethylenetetramine ($C_6H_{12}N_4$)2; 99 %, CAS: 100-97-9), both from Sigma Aldrich. Different parameters were tested: synthesis time (5 min, 15 min, 30 min, 45 min), temperature (70 ºC, 100 ºC, 130 ºC, 150 ºC) and pH (7, 9, 11 and 12).[32]

The aqueous solutions of zinc nitrate and hexamethylenetetramine produce the following chemical reactions[33]:

$$(C_6H_{12}N_4) + 6H_2O \rightarrow 6HCHO + 4NH_3 \quad (2.1)$$

$$NH_3 + H_2O \rightarrow NH_4^+ + OH^- \quad (2.2)$$

$$2OH^- + Zn^{2+} \rightarrow ZnO(s) + H_2O \quad (2.3)$$

The ZnO obelisk NRs were grown in an aqueous solution of 0.1 M of zinc nitrate hexahydrate ($Zn(NO_3)_2{\cdot}6H_2O$; 98%, CAS:10196-18-6) and 0.02 M ammonium chloride (NH_4Cl; 25%; CAS: 1336-21-6) from Sigma Aldrich and Carl Roth respectively. The pH

of the solution was adjust to 10.5 using ammonia.[34] The obelisk nanorods were synthesised at 100 ºC for 15 min.

For the growth of ZnO nanostructures, a seeded substrate (20 x 20 mm) was placed face down in the vessel. The synthesis were carried out in a microwave Discover SP, from CEM, with a microwave power of 40 W. After each process, the materials were cleaned with isopropyl alcohol and deionized water.

2.3 Deposition of Ag nanoparticles

The nanoparticles were formed using electron gun-assisted evaporation technique (Figure 2. 1). The temperature was kept at 150 ºC during the thermal evaporation of Ag mass-equivalent layer thickness (2, 4, 6 and 8 nm), with a deposition pressure of 10^{-5} mbar at a deposition rate of 0.07 nm·s^{-1}. The thickness and growth rates were inferred by a calibrated quartz crystal detector.

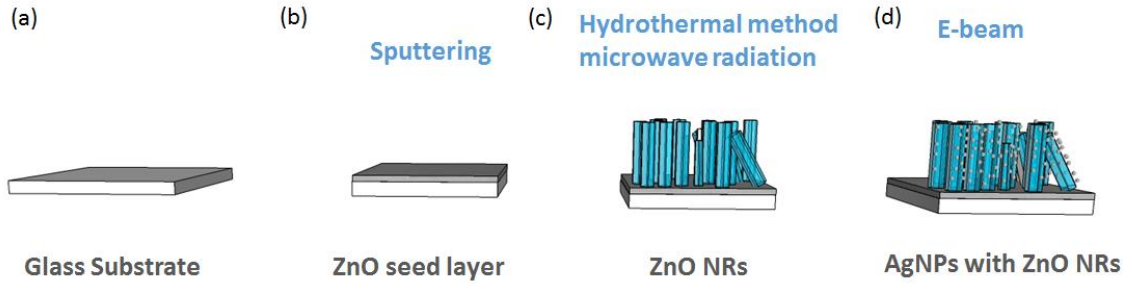

Figure 2. 1 - Schematic of production of ZnO NRs with *Ag NPs*: a) glass substrate; b) sputtering of ZnO seed layer on the glass substrate; c) growth of ZnO nanorods by hydrothermal method assisted by microwave radiation; d) e-beam silver film and formation of *Ag NPs*.

2.4 SERS Analyte

Tetraethylrhodamine hydrochloride (Rhodamine 6G – R6G) was purchased from Sigma Aldrich without further purification. Due to its high Raman cross section, this compound is commonly used as an analyte to evaluate SERS activity in the substrates. Concentrations of R6G solution were from 10^{-3} M for the control and 10^{-6} M for all samples. The substrates were prepared for SERS analysis by drop casting 2 µL of R6G solution onto the substrates, Figure 2. 2.[35]

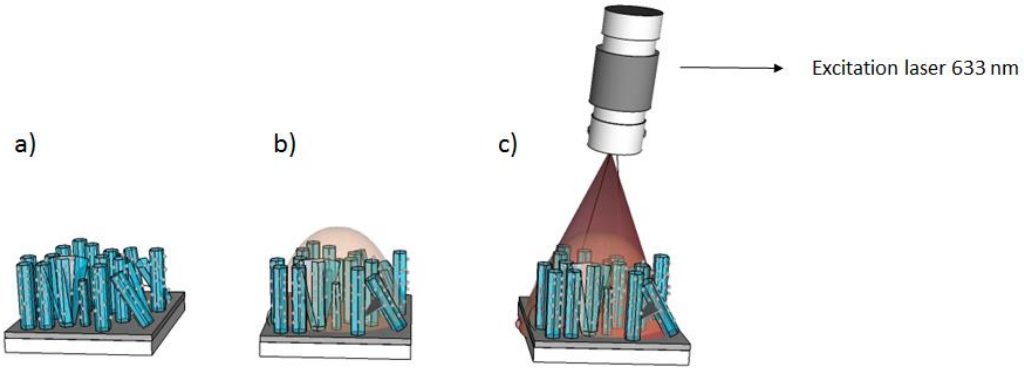

Figure 2. 2 - Schematic of SERS platform analysis with R6G: a) SERS platform of ZnO NRs with *Ag NPs*; b) Drop of 2 µL of R6G onto SERS platform; c) SERS signal measurement with excitation laser 633 nm.

2.5 Fabrication of the Microfluidics chip

The PDMS was prepared by mixing the base and the curing agent in a 10:1 ratio of weight. The mixture was stirred and degassed in a vacuum desiccator for 1h. Afterwards, the PDMS was poured into a Petri dish, and degassed again to remove the bubbles and thermally cured on a levelled hot plate at 80 ºC. Following, the microfluidics layout was etched by a CO_2 Laser (10.6 µm), VLS universal system 3.5 with the time and potency variation presented in attachment A.

The PDMS was bonded to glass by UVO (from Novascan PSD-UV) for 30 min, 5 cm away from the UV lamp. Directly after the treatment, the microfluidic device was put for 20 min at 70 ºC in a hot place to increase the bond strength of the PDMS with the glass substrate, Figure 2. 3.

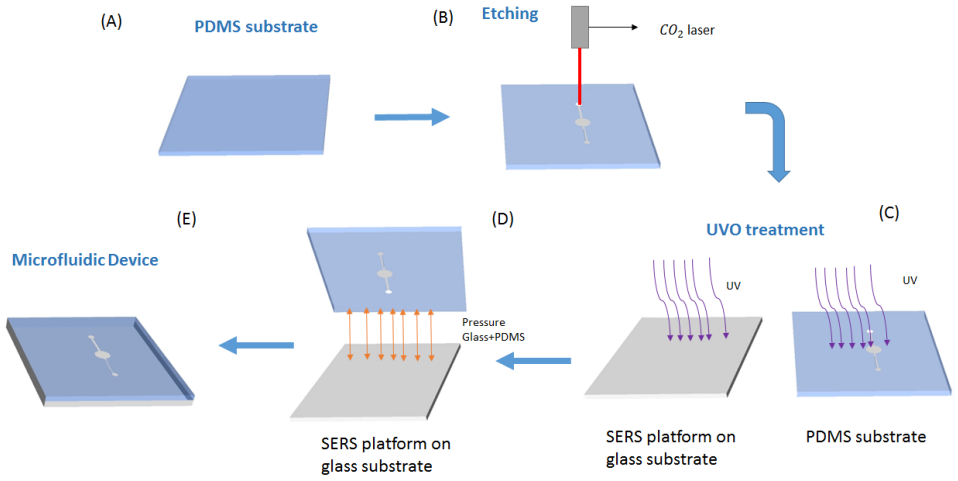

Figure 2. 3 - Schematic of the production of microfluidic device: (A) PDMS substrate; (B) Etching of the PDMS by CO_2 laser, making the microfluidics channel and well; (C) UVO treatment of PDMS substrate and glass substrate with SERS platform; d) Sealing of SERS platform with PDMS by applying pressure; (E) Microfluidics device.

2.6 Characterization techniques

Morphological characterization. The morphology of the NRs was examined by SEM-FIB using a Carl Zeiss AURIGA Crossbeam workstation instrument equipped with an Oxford X-ray Energy Dispersive Spectrometer. The dimensions of the ZnO nanorods were determined from SEM micrographs of 20 individual nanorods, using ImageJ software.

The crystallinity of the as-prepared materials was determined using a PANalytical X'Pert PRO MRD X-ray diffractometer, with a monochromatic Cukα radiation source (wavelength 1.540 598 Å). XRD measurements have been carried out from 10º to 60º (2θ), with a scanning step size of 0.016º.

Optical characterization. The UV-Vis spectroscopy was used to characterize the Ag NPs after their synthesis. The reflectance and transmittance spectra was obtained with UV-VIS-NIR spectrometer (Perkin Elmer lambda 950 UV/VIS/NIR) equipped with an integrating sphere, in the wavelength range of 300 – 1100 nm.

Raman measurements. Raman spectroscopy measurements were obtained with a Labram 300 Horiba Jobin Yvon equipped with an air-cooled CCD detector and a HeNe laser operating at 1750 µW of 632.81 nm laser excitation. The laser beam was focused with a 50x Olympus objective lens (N10.6 LPMPLAN FL N). An integration time of 5 scans of 25 seconds each was used for all measurements, with wavelength range of 1000 – 1700 nm.

The average enhancement factor value was calculated by measuring three different drops of R6G for each SERS platform.

3 Results and discussion

In this chapter the results from the developed work are presented and discussed. This project had the main objective of study the production of SERS substrates using ZnO NRs coated with Ag NPs aiming to maximise their SERS efficiency, and to apply them in a microfluidics chip, to test its viability. Hence, different synthesis parameters of ZnO NRs were tested, followed by morphological, structural and optical characterization through SEM, DRX and UV-Vis spectroscopy respectively and finally Raman spectroscopy was used to analyse SERS efficiency.

3.1 Morphological characterization

In order to study the ZnO NRs produced by hydrothermal growth assisted by microwave radiation, different parameters were tested, such as synthesis temperature, time, pH and ZnO seed layer thickness. The morphology and the ZnO NRs distribution was observed by SEM images.

3.1.1 Effect of temperature and time on the ZnO NRs Synthesis

In Figure 3.1 it is showed the SEM image of the ZnO NRs growth using different synthesis times (5, 15, 30 and 45 min) and synthesis temperatures (70, 100, 130 and 150 ºC).

To obtain the density and dimensions of the ZnO NRs fabricated, the SEM micrographs were studied by Image J software. In Figure 3. 2, shows the obtained density, Figure 3. 3 and Figure 3. 4 the obtained dimensions (table with dimensions in attachment B). For each sample 20 NRs were measured, as already described in the literature.[23]

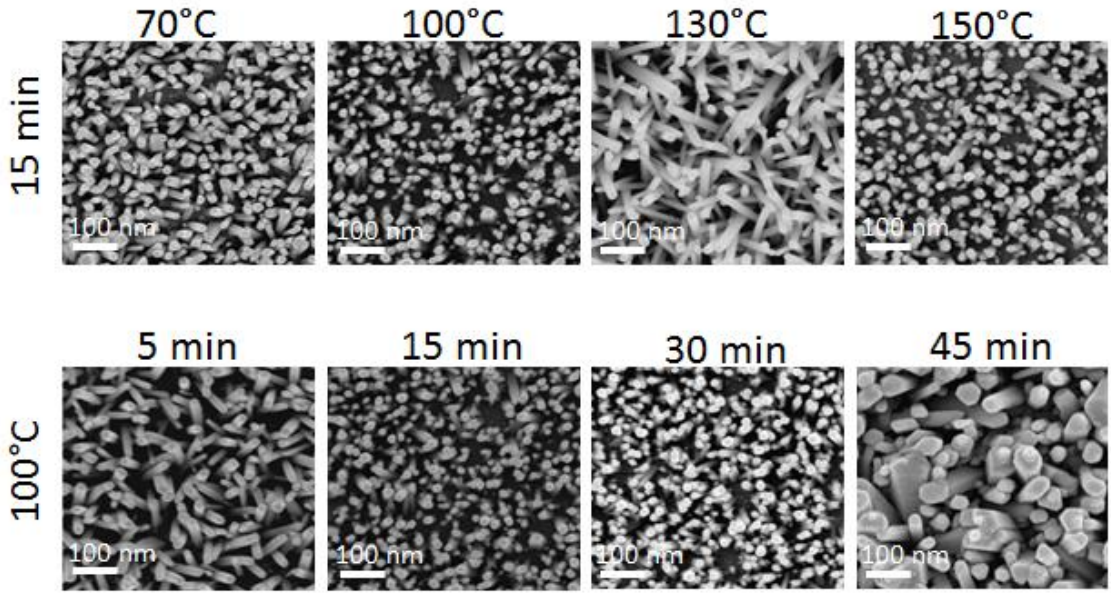

Figure 3.1 - SEM images taken from the top of ZnO NRs produced by hydrothermal growth at the indicated times and temperatures.

It was observed that by increasing the synthesis temperature from 70 ºC to 100 ºC there was a significant growth of the length of ZnO NRs, around 200 nm. For higher temperatures (130 and 150 ºC), the ZnO NRs did not show a dramatic increase of the growth, leading to a stagnation phase after reaction, possibly because the reagents reached a maximum point and the growth of the NRs stalls, Figure 3. 3. The diameter remained slightly the same. As the synthesis time and temperature increased, the density of nanorods per area decreased (Figure 3. 2 a, b). Simultaneously, as the time and temperature of the NRs synthesis are increased, the occupied area of NRs *per* μm^2 also increase. Moreover, higher synthesis temperature and time, the longer and wider are the ZnO nanorods, leading to a higher occupation of the glass substrate, with a smaller density.

At 130 ºC it was noticed that the NRs presented a less aligned formation when compared to the others. This phenomenon is possibly due to the heating rate of the synthesis, it has not been described in the literature.

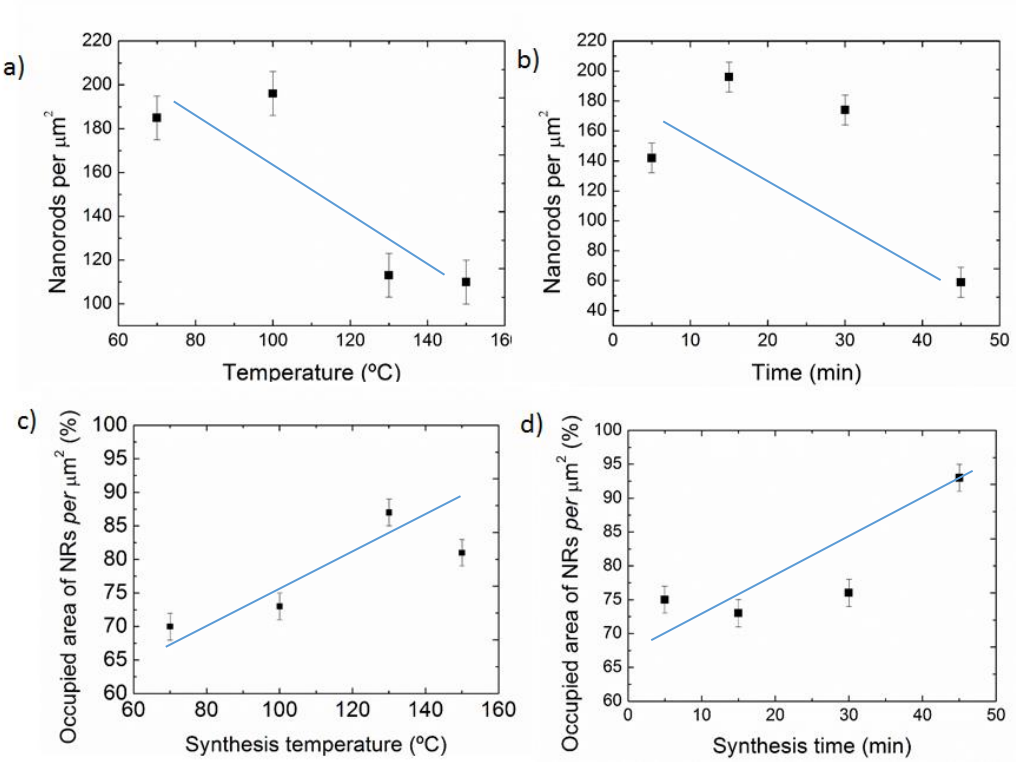

Figure 3. 2 - Changes in density with: a) number of NRs *per* µm^2 with different synthesis temperature; b) number of NRs *per* µm^2 with different synthesis time; c) area occupied by NRs with synthesis temperature; d) area occupied by NRs with synthesis time.

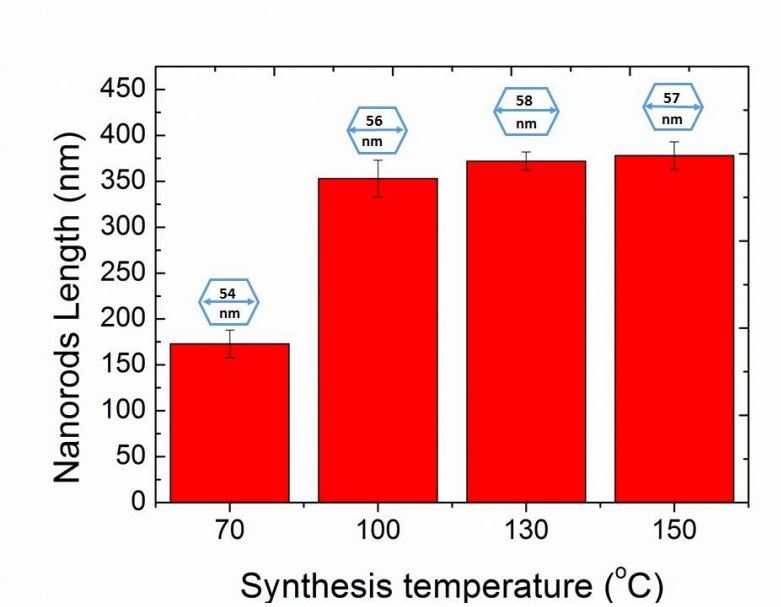

Figure 3. 3 - Variation of ZnO NRs length and diameter with synthesis temperature.

On the other hand, when the temperature was constant and the synthesis time increased (Figure 3. 4), the diameter of the ZnO NRs increased from 45 nm to 153 nm. This

significant increase of diameter is due to Ostwald ripening effect, where the tiny crystallites nucleate first followed by the growth of the larger particles due to the energy difference between large and smaller particles.[36,37] However their length did not change significantly after 15 min.

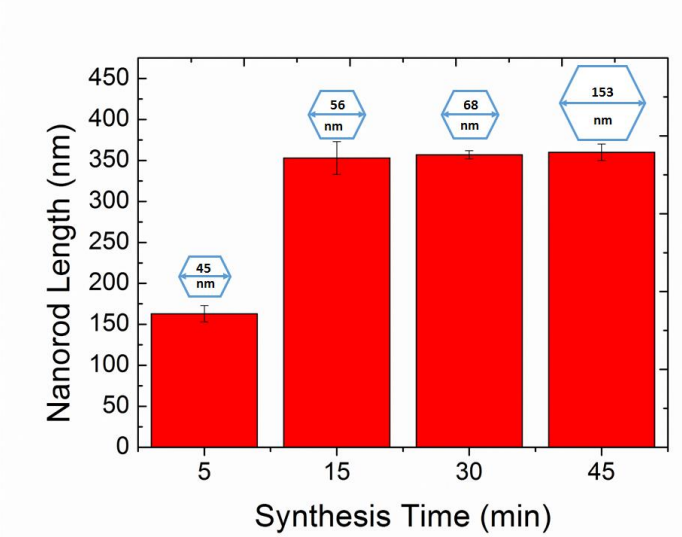

Figure 3. 4 - Variation of NRs length and diameter with synthesis time

Hence the ZnO NRs showed a preferential growth toward vertically and after stabilizing the NRs expand horizontally, has it has been described in the literature.[22,38–42]

3.1.2 Effect of pH on the ZnO NRs synthesis

In the literature is referred that the increasing the pH of the synthesis solution, to grow ZnO NRs by hydrothermal method in the oven, will lead to flower-like nanostructures.[21,43,44] Thereby, a study of the influence of pH on ZnO NRs using hydrothermal growth, assisted by microwave radiation, was performed by adding ammonia to the standard solution, (at constant synthesis time – 15 min - and temperature – 100 ºC). The results are presented in Figure 3. 5, where four different pH values were used for the ZnO NRs synthesis (7, 9, 11 and 12).

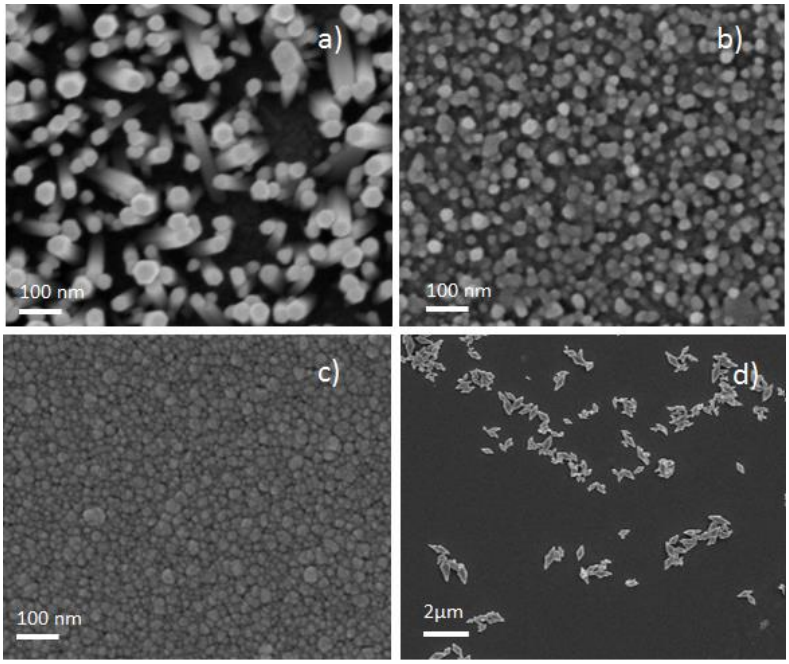

Figure 3. 5 – SEM images of ZnO NRs synthesized with different pH values: a) 7; b) 9; c) 11; d) 12.

With the rise of the pH value of the synthesis solution, using ammonia, the ZnO NRs morphology changed considerably. At a pH value of 9, Figure 3. 5 b), the NRs were significantly smaller (compared to pH 7, Figure 3. 5 a); at pH 11 (Figure 3. 5 c) there was no growth of structure, and at pH 12 (Figure 3. 5 d) there are the appearance of small structures dispersed in the substrate was observed. The results are in accordance to what is described in the literature.[43] For the formation of NRs it is influenced by a competition between crystal growth and etching, therefore, neutral or acidic conditions are required for its formation. According to the literature, by increasing the pH, the morphology of the NRs changes from rods (pH value of 7) to flower-like (around pH 12),[43] however, the fully grown flower like nanostructures were never obtained.

3.1.3 Effect of ZnO Seed layer thickness on the ZnO NRs synthesis and structural analysis

The third parameter evaluated on ZnO NRs synthesis was the seed layer with four different thicknesses: 100 nm and 150 nm, 200 nm and 300 nm. The crystallinity and the crystal planes the ZnO NRs were analysed by their respective XRD patterns, Figure 3. 6.

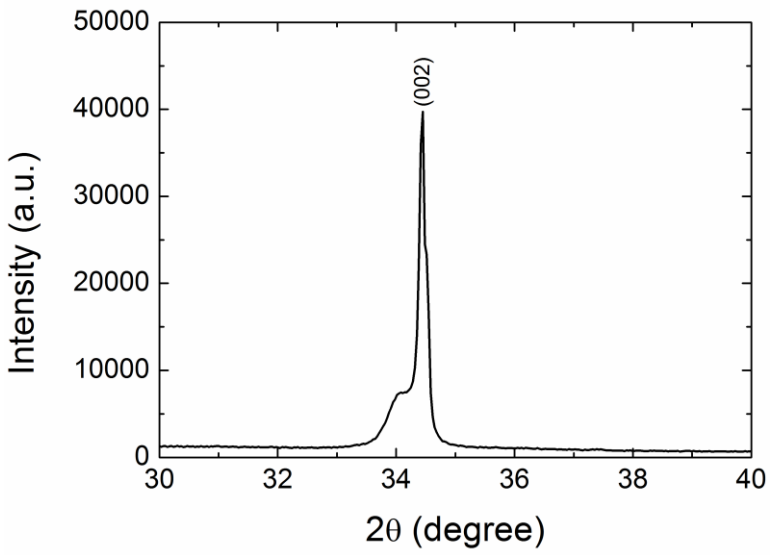

Figure 3. 6 - Representative XRD pattern of ZnO NRs; indexed peaks corresponding to the typical wurzite hexagonal structure.

Figure 3. 6 shows a representative spectrum of all samples with different ZnO NRs obtained by the different synthesis. The sample shows one peak at 34.45 degrees corresponding to hexagonal wurzite ZnO crystalline structure, with lattice constants of *a*=0.3296 nm and *c*=0.52065. At 34.11 degrees, there is a small protuberance due to the effect of the seed layer (attachment C). All the samples shown have (002) as the preferred orientation, which is in good agreement with literature values.[21] The observed high intensity and narrow spectral width of the XRD pattern prove that the ZnO NRs are highly crystalline and with no impurities detected.[22]It was observed that as the seed layer thickness increased, the intensity of the signal also increased due to its higher crystallinity, has already reported by literature (attachment C).[21,22,40]

The grain size D, of the ZnO seed layers was calculated by XRD using Scherre's equation:

$$D = 0.94 \times \lambda \times \beta \times cos\theta \qquad (3.1)$$

where λ is the wavelength of the X-ray radiation, β is the full width at half maximum (FWHM) and θ the Bragg's angle. In Figure 3. 7, it is showed the calculated grain size for each seed layer thickness.

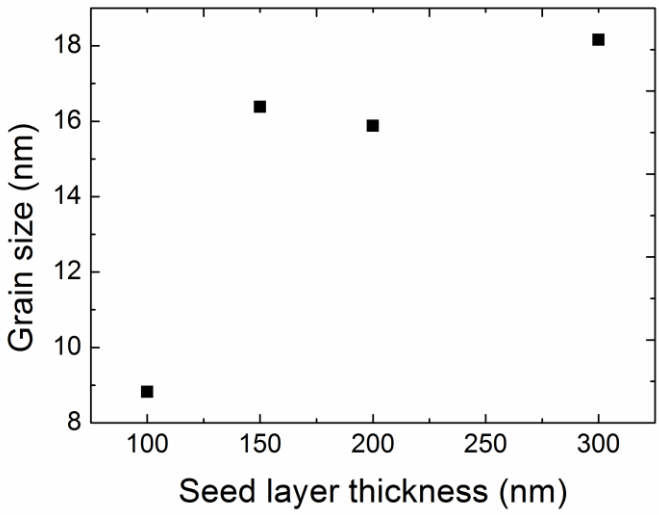

Figure 3. 7 - Variation of ZnO grain size with seed layer thickness.

As expected from the literature, by increasing the seed layer thickness, the grain size also increases.[40] Also crystallinity of the ZnO seed layer is improved (attachment C), making the NRs more aligned, as it can be observed in Figure 3. 8.[45–47]

The diameter and length of the NRs with different seed layer thicknesses was measured by ImageJ surface imaging and cross-section respectively, Figure 3. 8.

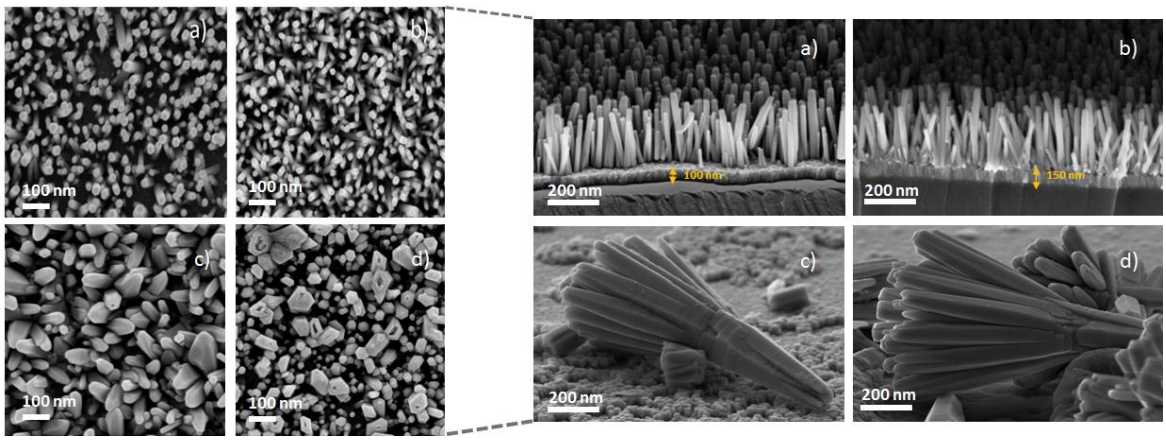

Figure 3. 8 - SEM image of ZnO NRs grown with different seed layers thickness: a) 100 nm; b) 150 nm; c) 200 nm; d) 300 nm (*left* side); SEM images of cross section of ZnO NRs with different seed layer thicknesses. a) 100 nm; b) 150 nm, c) 200 nm; d) 300 nm (*right side).*

In Figure 3. 9, it is possible to observe the measured dimensions of the NRs.

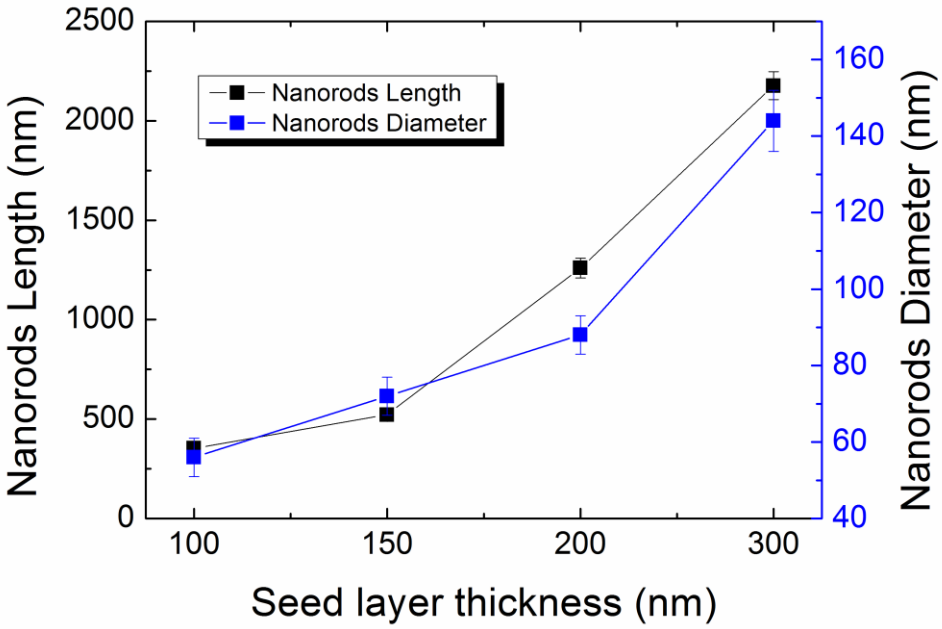

Figure 3. 9 – Variation of ZnO NRs length and diameter with seed layer thickness. (Guide lines for visual aid).

When measuring the dimensions of the NRs, it was expected an increase of the diameter as the seed layer thickness increased, due to the larger grain size. The length of the ZnO NRs, in this case, also increases with the seed layer thickness, which contradicts the results reported in the literature for hydrothermal growth by conventional heating, where NRs length decreases with the seed layer thickness. There were no reports regarding the effect of the seed layer on the length of ZnO NRs growth by microwave assisted synthesis.

Also, as the seed layer thickness decreases, there is an increase of density of the NRs, seen Figure 3. 2. As the grain size increases, there are less nucleation points, leading to a smaller density of NRs.[32,40,45]

The growth rate of the ZnO NRs rises significantly with the seed layer thickness, Figure 3. 10, suggesting that the seed layer thickness represents a crucial parameter in ZnO NRs growth. The changes of the NRs dimensions obtained by different seed layer thicknesses surpassed greatly the other synthesis parameters.

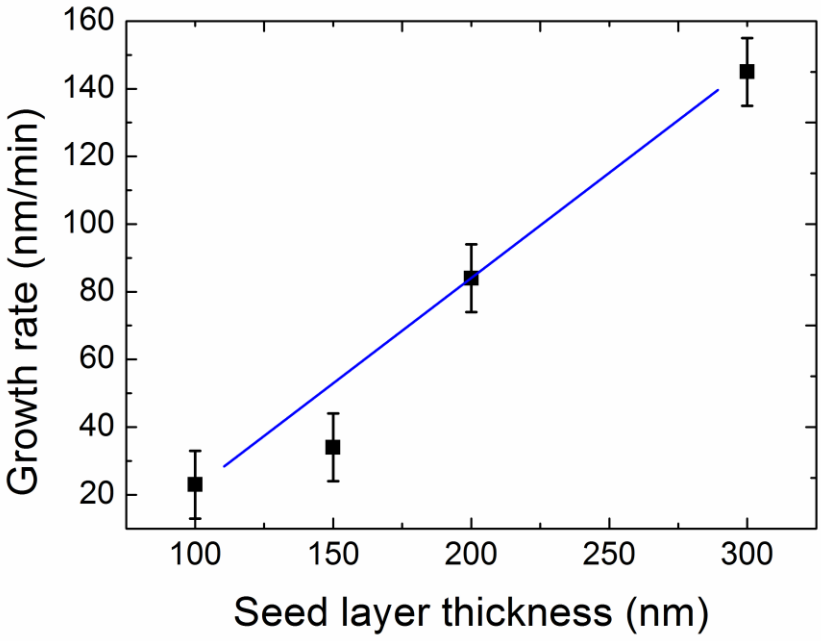

Figure 3. 10 - Growth rate of ZnO NRs with different seed layer thicknesses. (Trend line for visual aid).

3.2 Characterization of Ag nanoparticles

After ZnO NRs morphology studies, the samples with different morphologies were submitted to PVD for Ag NPs deposition. This last experimental step originated the SERS platforms. The samples were chosen for its higher available area for Ag NPs coupling, leading to more NPs *per* NRs.

The samples chosen for the following work were Ag NPs with different diameters: 2, 4, 6 and 8 nm onto NRs synthetized with different temperatures (70, 100, 130 and 150 ºC), with synthesis time of 15 minutes. For the study of the ZnO seed layer thickness (100, 150, 200 and 300 nm) and the obelisk nanorods, only the *Ag NPs* with 6 nm were deposited.

The distribution of the NPs throughout the NRs varies with Ag thickness. In Figure 3. 11, the different NP thickness are shown, using the same NR dimensions (synthesis time of 15 min at 100 ºC).

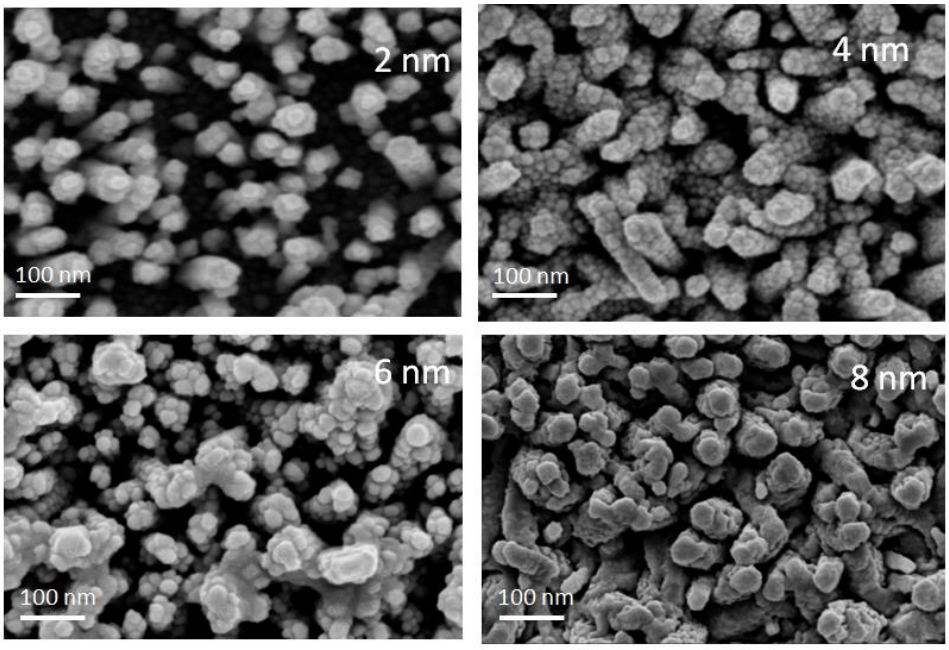

Figure 3. 11 - SEM image of ZnO NRs with different Ag NPs thickness of 2, 4, 6 and 8 nm.

The SEM image of Figure 3. 11 revealed a highly dense and uniform distribution of Ag NPs without large-scaled agglomerates for the NP with 2 and 4 nm thickness. The nanoparticles with 6 and 8 nm thickness, on the other hand, shown the formation of agglomerates.

After PVD, the LSPR spectral position and the wavelength range of the SERS substrates was determined. Absorptance spectra (Figure 3. 12) were determined from the total reflectance (R_{tot}) spectra and total transmittance (T_{tot}) and was calculated using the following equation:

$$Absp = 100 - R_{tot} - T_{tot} \qquad (3.2)$$

There are two characteristic bands present in the absorptance spectra of the SERS substrates: the quadrupole resonances and the dipole resonances. The shorter wavelength peaks correspond to the quadrupole resonances (around 350 nm), whereas the broader peaks, at longer wavelengths, correspond to the dipolar resonances of the Ag NPs. The dipole resonance is due to the collective oscillation of the electrons. This oscillation is determined by four factors: the density of electrons, the effective electron mass, and the shape and size of the charge distribution.[8,48,49] Hence, the increase of the Ag mass thickness leads to an increase in the average particle size (Figure 3. 12 b), which results in a red shift, from 450 nm for the Ag 2 nm to 470 for the Ag 8 nm, and in the broadening of the LSPR peaks.[8,50]

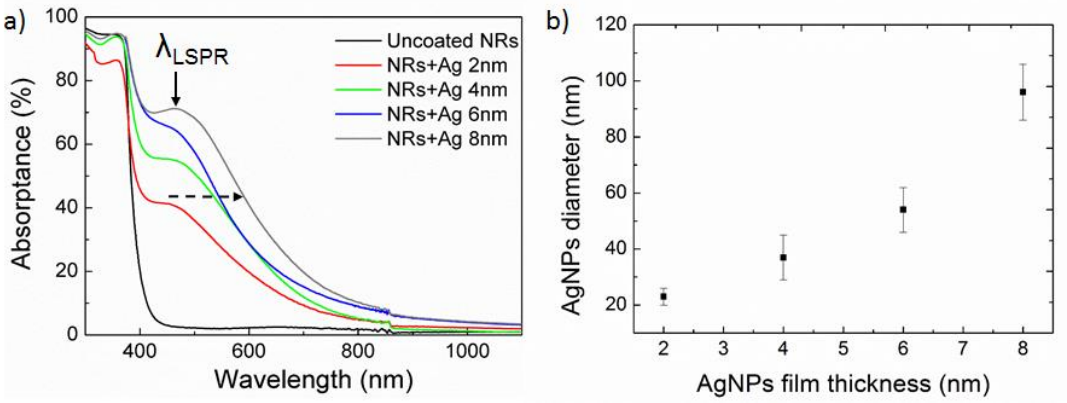

Figure 3. 12 - a) Absorptance spectra of SERS substrates with uncoated ZnO NRs and ZnO NRs with 2 nm, 4 nm, 6 nm and 8 nm mass thickness of silver. b) *Ag NPs* diameter with *Ag NPs* film thickness.

Theoretically to obtain high enhancements require that the incident radiation and the Stokes Raman shifted radiation are in resonance with the metal nanostructure.[9]

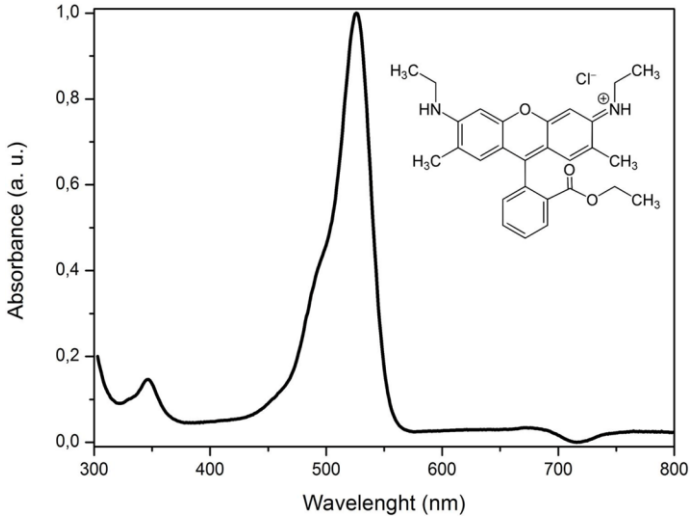

Figure 3. 13 - UV-Vis absorption spectrum of R6G with its molecular structure inset.

3.3 Raman and SERS signal of Rhodamine 6G

For the present work, R6G was used as the model analyte due to its large cross-section and strong SERS signal. The strong visible absorption of R6G in aqueous solution has a maximum around 530 nm (Figure 3. 13). When R6G is excited with visible light at 532 nm, leads to larger enhancements due to a combination of the SERS effect that originates from surface plasmon excitation, and molecular resonance Raman effect. However,

it can generate high fluorescence yield which would prevent the observation of the Raman spectrum.[35,51]Therefore, the excitation laser wavelength used in this project was 633 nm.

The spectra presented in Figure 3. 14 corresponds to the Raman spectrum of a 10^{-3} M R6G aqueous solution drop in a glass slide and the SERS spectrum of 10^{-6} M R6G aqueous solution on a ZnO NRs with Ag NPs SERS substrate using the 633 nm wavelength excitation laser.

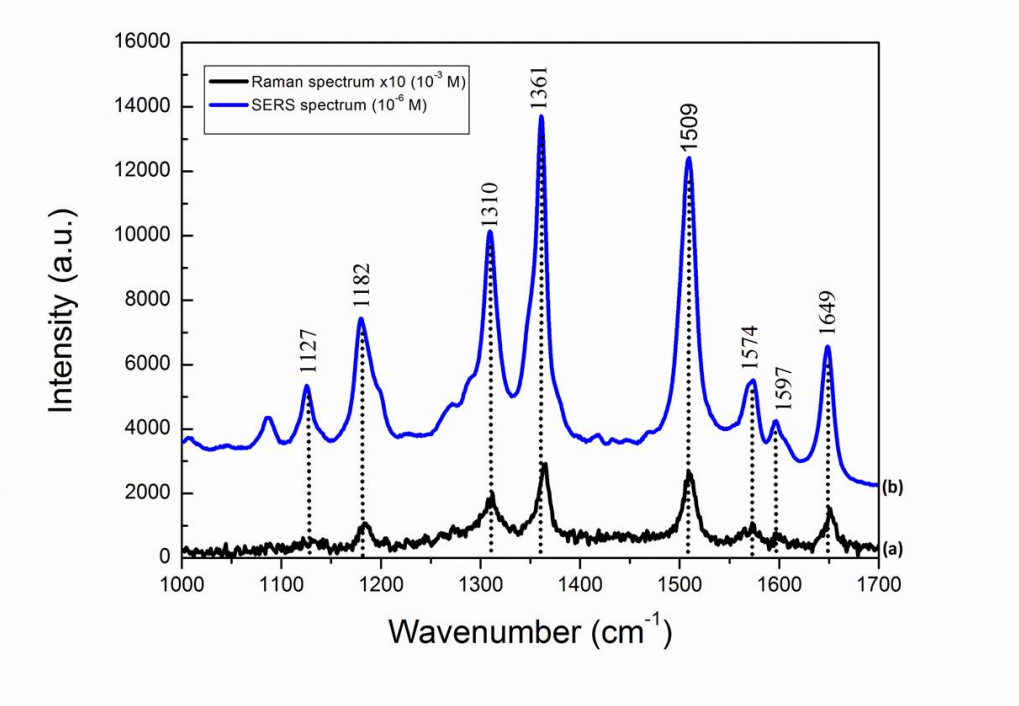

Figure 3. 14 - Raman and SERS spectrum of R6G. (a) Raman spectrum of 10^{-3} M R6G aqueous solution (x10 magnified) and (b) SERS spectrum of 10^{3} M R6G aqueous solution on glass substrate with Ag NPs@ZnO NRs under 633 nm laser excitation.

In both Raman and SERS spectra, the two main vibrational bands correspond to the aromatic C-C stretching modes at 1361 and 1509 cm^{-1}. The assigments of the vibrational bands are shown in table Table 3. 1.[35]

Table 3. 1 - Vibrational bands assignments for R6G.

Experimentally observed bands (cm^{-1})		Assignment
Raman	**SERS**	
	1030	
	1127	in plane C-H bending
1310	1310	In plane xanthene ring breathing, N-H bending, CH_2 waggling
1362	1361	Xanthene ring stretching, in plane C-H bending
1509	1509	Aromatic C-C stretching, xanthene ring stretching, C-N stretching, C-H bending, N-H bending
	1574	Xanthene ring stretching, in plane N-H bending
1597	1597	
1649	1649	Xanthene ring stretching, in plane C-H bending

As can be observed the vibrational bands of the two spectra are coincident, however the SERS signal is more intense and presents a lower noise, despite using a three orders of magnitude lower concentration of R6G. This image clearly illustrates the effect obtained by a good SERS substrate on the Raman spectrum of an analyte.

3.4 SERS assays for ZnO NRs with Ag NP

To compare the intensity of the signal from SERS substrates to normal Raman EF values are usually used. In this project, the SERS assays were performed by testing different Ag NPs size with the different ZnO NRs obtained, using drops of 2 µL of R6G solution.

The areas of the vibrational bands at 1360 cm^{-1} and 1509 cm^{-1} from R6G SERS spectra were used to calculate the average EF values. Using a concentration of 10^{-6} M the following histograms (with the four different Ag thicknesses) with their average EF values and respective standard-deviations (SD) were calculated for the 1509 cm^{-1} vibrational band (the complete histograms with 1360 cm^{-1} and 1509 cm^{-1} are presented in the attachment D).

It was expected for the average EF values to increase with the longer ZnO NRs due to an increase of Ag NPs density *per* area and therefore a higher number of Ag NPs would contribute to the SERS signal.

As it can be seen in Figure 3. 15, the expected behaviour did not occur (only EF for the vibrational band of 1509 cm^{-1} are represented). Using the same NPs size, with different NRs length, hence more Ag NPs *per* area of NRs, there was not a significant difference of the average EF values or a clear correlation between NR length and NP size. All average EF values for the different samples were localized between 10^5 and 10^6. A possible explanation for these results can be attributed to the vertical orientation of the majority of the NRs, hindering the SERS signal from the Ag NPs located at the bottom of the NRs. For the 2 nm mass thickness of Ag (Figure 3.15 a) there is a tendency for the increase of EF with the NRs length, this is attributed to the lower size of the Ag NPs that allow more signal from the bottom of the NRs to contribute to the global EF value. The same can be observed for the 4 nm mass thickness of Ag (Figure 3.15 b) up to 378 nm of NRs length. For larger NPs the effect is lost, and no correlations are found.

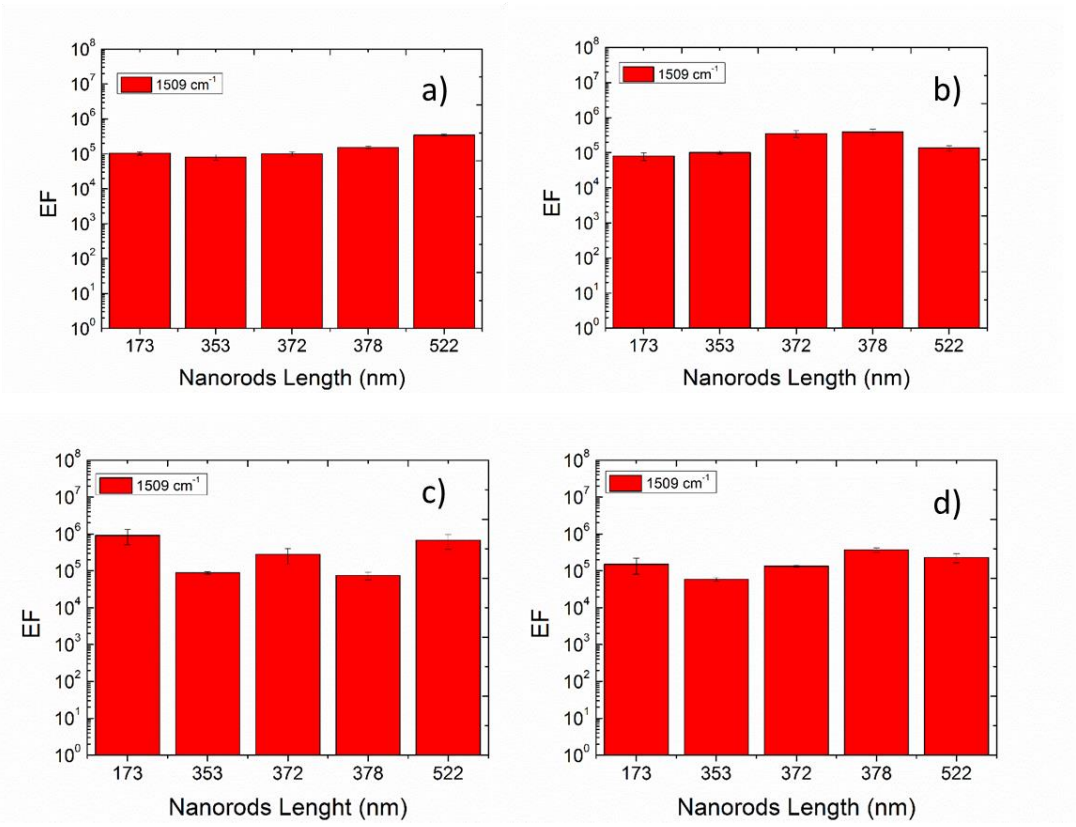

Figure 3. 15 - Average EF calculated using the vibrational bands areas at 1509 cm^{-1} for: a) 2 nm Ag NPs; b) 4 nm Ag NPs; c) 6 nm Ag NPs; d) 8 nm Ag NPs.

Additionally it was studied the average EF values with the different seed layers thickness, using Ag NPs with 6 nm thickness. Results are presented in Figure 3. 16.

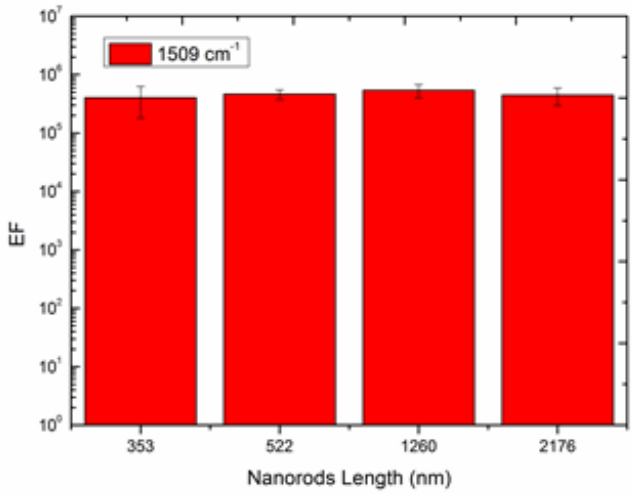

Figure 3. 16 - Average EF values with Nanorods length.

As it was expected from the results obtained previously, the average EF values remained approximately the same for the different nanorods length.

For a better understanding of these results, Figure 3. 17 elucidates the fabrication process of the SERS nanostructures.

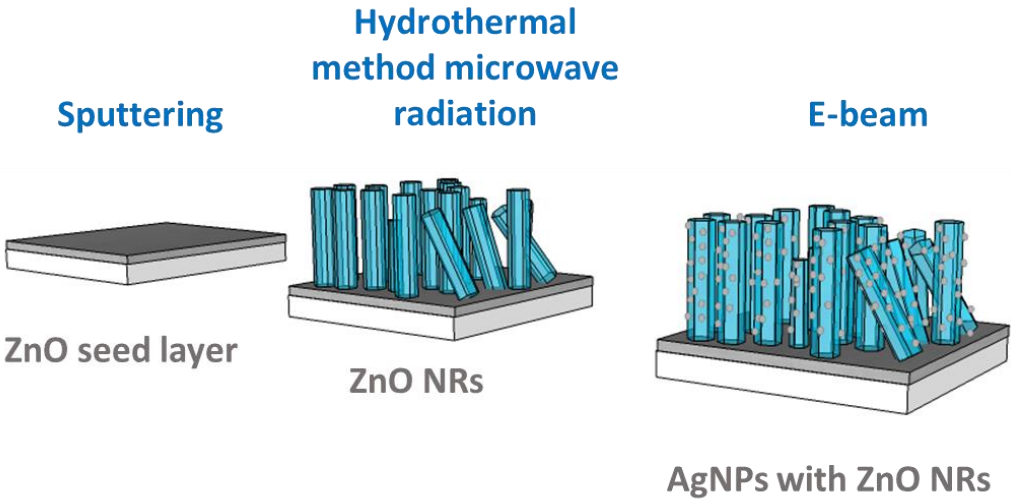

Figure 3. 17 - Schematic image of the fabrication of an arrays of ZnO NRs decorated with Ag NPs on glass substrate (*adapted from*[52]).

The ZnO seed layer was deposited by sputtering, making it a highly homogeneous substrate for the growth of the NRs. Consequently, the majority of the nanorods grew parallel to each other, by the hydrothermal method. Therefore, the nanorods are well

aligned with the nanoparticles attached throughout their surface. Possibly, the values of the average EF for different NRs was not affected by the length of the nanorods because of the polarization of the excitation laser, as it is known that near field distribution (*hot spots*) have a strong dependence on polarization.[53] Since NRs are well aligned, the laser could only reach the superficial NPs coupled in the NRs. Therefore, only the *hot spots* localized in the surface were activated, resulting in the same average EF value for the different samples tested.

In terms of Ag thickness variation, for the same NR, it was expected that a higher thickness would result in a creation of clusters, and eventually, the formation of films, which would lead to a loss of the LSPR and consequently a decrease of the EM. However, although the Ag NPs showed an increase of aggregation, they did not change drastically the efficiency of SERS (Figure 3. 11 and attachment E).

Due to the number of available NPs in the NRs for enhancing the SERS signal, not being considerably different, even though the longer NRs have more nanoparticles *per* nanorod, the NPs in the same NR create *hot spots* parallel to the laser and, therefore, they do not increase the average EF values. Hence, the thickness of the NP does not impact significantly the average EF value, particularly for the longer NRs and NPs above 4 nm Ag mass film thickness as explained above.

If only the superficial *hot spots* are activated in the earlier measurements, it was tested a sample of ZnO NRs synthetized at standard conditions (100 ºC; 15 min with seed 100 nm thickness) with the previously used inclination and a new inclination by tilting the sample in and angle of 45º (Figure 3. 18).

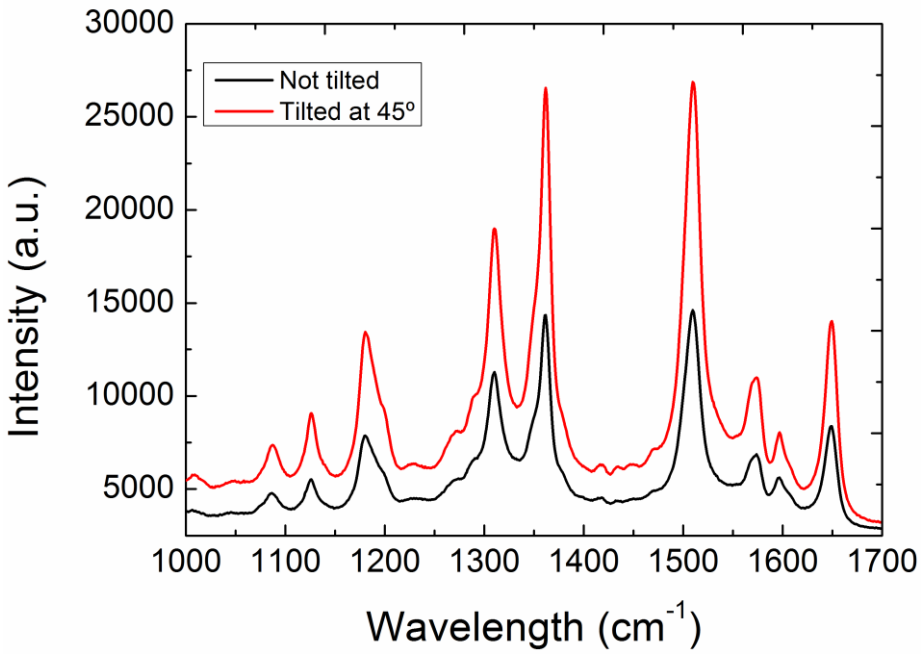

Figure 3. 18 - SERS spectrum of R6G using different inclination.

In Figure 3. 18, it is possible to confirm that with a different inclination the signal intensity increases considerably. The respective EF value obtained was around 10^6, which, although, was not significantly higher, it was highest EF value attained in the present work.

3.5 SERS efficiency with Obelisk Nanorods

In order to determine the influence of the NRs top morphology a different study was performed using NRs with obelisk form (Figure 3. 20). In this case, to obtain the obelisk tips, it was used a different solution, where hexamethylenetetramine was replaced with ammonium chloride.[33] The obelisk NRs were grown at a temperature of 100ºC for 15 min.

The crystallinity and crystal planes of the obelisk ZnO nanorods were analysed with XRD, Figure 3. 19.

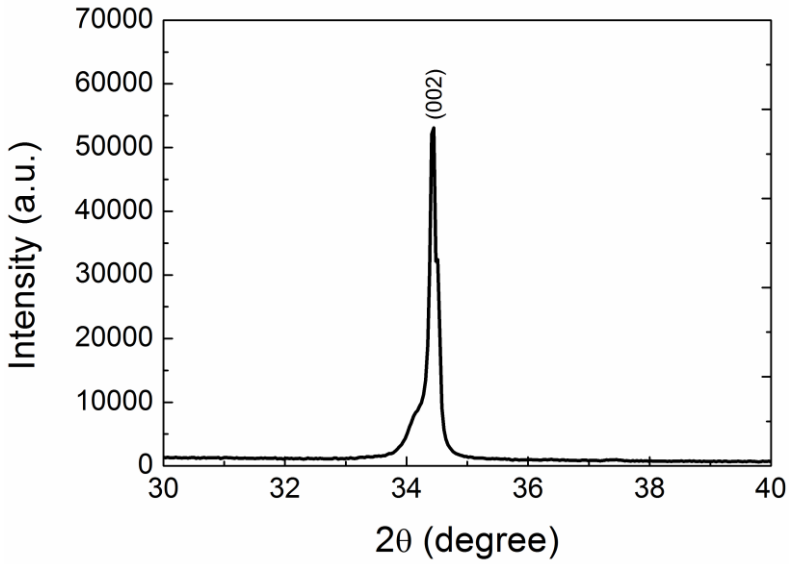

Figure 3. 19 - XRD pattern of ZnO obelisk NRs; indexed peak corresponding to the typical wurzite hexagonal structure.

By magnifying the spectra it is possible to observe a single peak at 34.25 degrees, corresponding to the crystallographic plans of the hexagonal wurtzite ZnO structure.[54] As in the previous samples, the obelisk NRs also showed a small protuberance at 34.10 degrees, due to the seed layer. The sample showed (002) as the preferred orientation, which is in good agreement with literature values[21]. The high intensity of the peak indicates that the NRs are well aligned and perpendicular to the substrate, as it was observed in SEM images. The high intensity and narrow spectral width show that the nanorods are highly crystalline and with no impurities detected.[22]

As an alternative to use Ag NPs inter-gaps as *hot spots*, the tips of the NR coated with a 14 nm Ag film were used, as it is known that *hot spots* also appear in sharp protuberances. It was chosen an Ag film with 14 nm in order to be enough to obtain a strong electromagnetic field, without losing the cone shape at the tip of the nanorod. For comparison of the average EF value, it was deposited Ag NP with 6 nm thickness, (Figure 3. 20), since it was the thickness with the highest average EF value for the NRs previously studied.

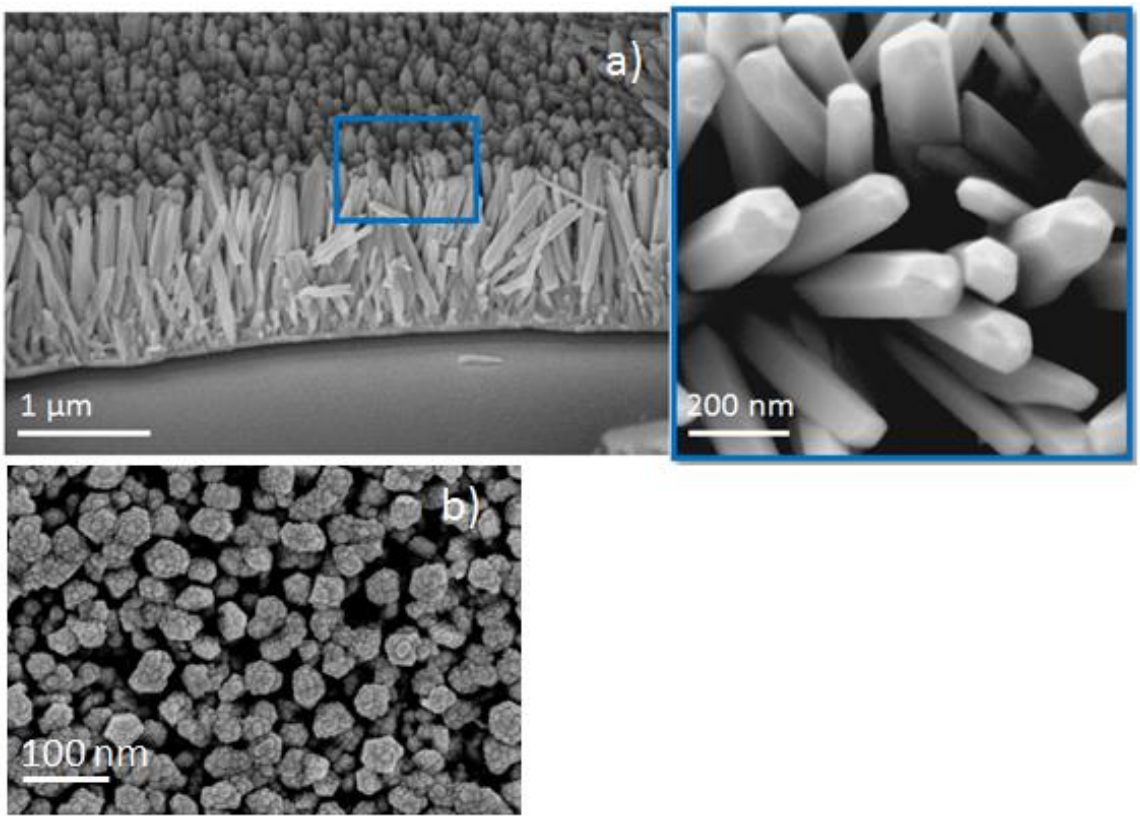

Figure 3. 20 – SEM images of obelisk nanorods with: a) Ag film. High and low magnification; b) Ag NPs deposited by PVD.

In this case, the length obtained when compared with the average length of the previous studied NRs (360 nm) is expressively higher, and the NRs showed a very high density. The density of obelisk nanorods was higher compared to the standard hexagonal NRs, 311 NRs *per* μm^2, as the occupation of NRs *per* μm^2 was around 95%.

Table 3. 2, shows the dimensions of the obelisk nanorods.

Table 3. 2 – Dimensions of obelisk nanorods.

	Length (nm)	**Diameter (nm)**
Obelisk NR	1500	171.9

The Ag NPs obtained in the obelisk ZnO NRs were uniform and had an average diameter of 63 nm.

In Figure 3. 21 it is compared the average EF value of obelisk nanorods coated with 14 nm Ag thin film, obelisk nanorods with NPs and the standard hexagonal nanorods with Ag NPs of 6 nm film thickness.

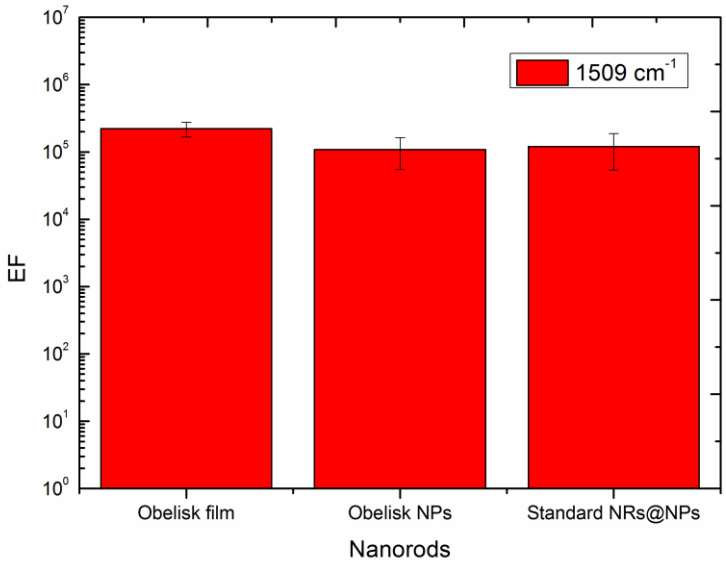

Figure 3. 21 – Comparison of the average EF values of obelisk Ag film with obelisk NPs and Standard hexagonal NRs with NPs.

The average EF values obtained between the obelisk film NR and the obelisk NP nanorods is approximately the same, around 10^6. This results are in agreement with those obtained in the standard hexagonal nanorods with NPs. In the case of the obelisk NRs with Ag thin film, the *hot spots* are localized only at the sharp protuberances of the nanorods, and in the obelisk NRs with Ag NPs, the *hot spots* occur in the inter-gaps of nanoparticles in different nanorods. The fact that the average value of EF for film and NP obelisk nanorods suggest that the number of active *hot spots* created in both is approximately the same. Therefore, like in the hexagonal nanorods, the *hot spots* are localized mainly in the superficial area of the ZnO Ag structure. Additionally, the enhancement created by the NPs on their own was similar to the enhancement created in the tips of the obelisk NRs.

3.6 Fabrication of PDMS microfluidics device

Knowing the inherent advantages of PDMS microfluidics devices (*e.g.* high precise control and portability), a device was assembled. Since the used SERS platforms have silver nanoparticles, the microfluidic device also minimise the oxidation of Ag and, consequently, degradation of the SERS platform.

First, using a CO_2 laser, the channels and well of the microfluidic devices were formed by etching of the PDMS substrate, using a determined power and velocity (45 W

and 0.05 s/cm respectively), Figure 3. 22. Second, using a UVO treatment (for 30 minutes), the PDMS was bonded to the glass substrate with the NRs previously grew at 100 ºC for 15min.

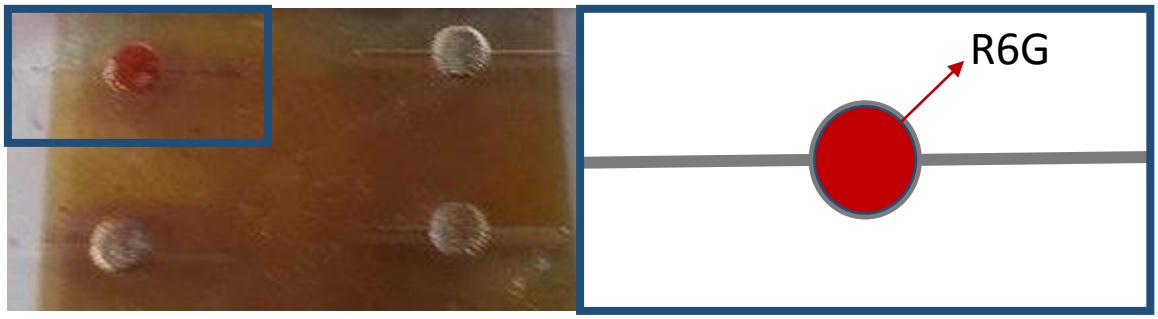

Figure 3. 22 - PDMS microfluidics device image (*left*) and its schematic with R6G (*right*).

The R6G was injected in the channel with a syringe and, with vacuum, pulled to the well. Table 3. 3 presents the diameter of the well and the channels, measured by confocal microscope.

Table 3. 3 - Dimensions of Microfluidics device.

	Well diameter (nm)	**Channel diameter (nm)**	**Channel depth (nm)**
Microfluidics device	$1x10^6$	341	161

First it was measured the background signal of the PDMS without R6G and after the SERS spectra of R6G with a concentration of 10^{-4} M, Figure 3. 23. It was chosen a concentration of 10^{-4} M, instead of 10^{-6} M, for a better perception of the injected R6G in the microfluidics channel (R6G at 10^{-4} M has a strong pink colour, which allows a visual control of the injection of the analyte in the channel).

Since the PDMS was etched using a laser technique, the walls of the channels and well presented a certain roughness. To decrease the formation of this roughness, instead of using laser, using photolithography technique could be a suitable solution for a smoother surface.

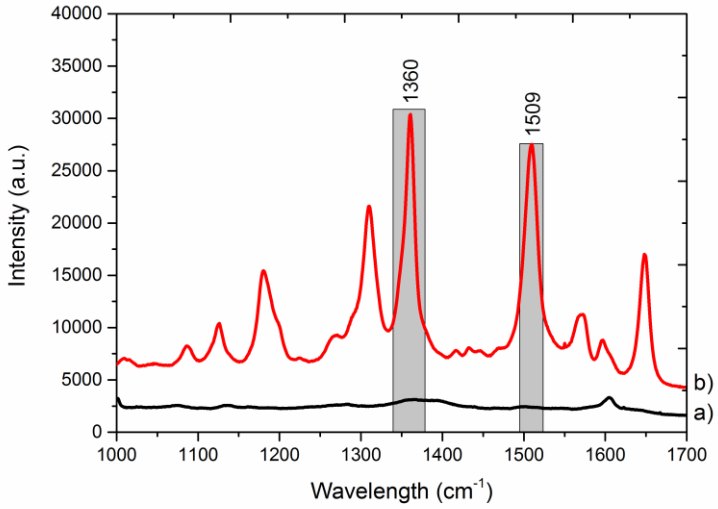

Figure 3. 23 - SERS spectrum of R6G in PDMS device. (a) Background spectrum of device without R6G; b) SERS spectrum of 10^{-4} M R6G in PDMS device under 633 nm laser excitation.

This spectra is in good agreement with the literature[35], where R6G can be easily identified.

Even though PDMS has its own Raman signal, it was possible to measure the R6G by using a confocal Raman microscopy. Where a confocal slit collets only the laser-induced signal from a distinct focal volume within the diffraction limit.[55]

4 Conclusion and Future Perspectives

The main objective of this project was to develop efficient nanostructures for SERS applications. For that, different parameters of hydrothermal growth synthesis of ZnO NRs were tested (temperature, time and pH), as well as different seed layer thicknesses (100, 150, 200 and 300 nm) with different Ag nanoparticles thickness (2, 4, 6 and 8 nm) deposited by PVD technique.

By increasing the synthesis temperature and time, there is a significant increase in the nanorods length and after an increase of the NRs width, due to the preferential growth ratio of the ZnO NRs. With longer synthesis times, the nanorods obtained have a wider diameter, indicating that after growing vertically, they expand horizontally.

When increasing the pH of the synthesis solution, flower petal like ZnO nanostructures were obtained (pH~12), while NRs formation stopped for pH higher than 7. The formation of ZnO NRs is determined by the competition between crystal growth and etching (caused by acidic conditions).

In the study of the influence of the seed layer thickness, it was possible to conclude that thicker seed layers led to higher crystallinity and larger grain size of the ZnO film. The length and diameter of the NRs increased significantly due to the larger grain size and Ostwald ripening effect. The increase of length with seed layer thickness is possibly due to the larger grain size and crystallinity, leading to a more stable and fast growth, although, it has not been reported yet in the literature.

The use of different ZnO NRs length had the intention of increasing the sensitive area for SERS, allowing the deposition of more nanoparticles, therefore, resulting in a formation of more *hot spots* and consequentially, an increased enhancement. However, there was no considerable change of enhancement with different nanorods length, using the same NP thickness. Possibly, since the NRs are vertically aligned and the excitation laser is perpendicular to the substrate, only the *hot spots* closer to the surface are activated, while the ones located in the lower NP are not. Here, the created *hot spots* are localized between the Ag NP of parallel NRs, while the gaps inter nanoparticles, of the same nanorod are not activated. This phenomenon has already been reported in literature, where the polarization of the excitation laser is stated to have a variance of four order of magnitude in the EF value.[12,20,53] In this present work, instead of changing the polarization of the excitation laser, as an alternative, the samples were tilted in an angle of 45º, which led to

an increase of the SERS signal. Thus, the homogeneity of the average EF values with different NRs length, is indicative of this behaviour. Still, the ZnO NRs showed to be a highly performing reproducible platform for SERS devices.

The study of Ag NPs thickness was tested with the purpose of determine the most efficient in SERS. Although the thicker NPs had a small formation of aggregates, it did not have a direct impact on the average EF value. Since the formation of aggregates would lead for a change of the LSPR, resulting in a change in the EF value. Still, all Ag N*Ps* thicknesses presented good average EF values, around 10^6 for a concentration of 10^{-6} M.

The ZnO obelisk nanorods presented a high density, around 95 % of area occupied by NRs. The average enhancement factor values for the obelisk nanorods with thin Ag film were considerable, around 10^6, similar to the obelisk nanorods with Ag NPs and the standard hexagonal NRs.

For a more precise control, manipulation and portability it was developed a PDMS microfluidics device. The device showed a good SERS efficiency, and the R6G was detected through the PDMS.

In conclusion, all SERS platforms obtained had good SERS efficiency. The overall enhancement factor values for every SERS platform were around 10^6, using a concentration of 10^{-6} M of R6G. It was successfully developed a promising microfluidics device, using the optimized ZnO NRs, where it was possible detected the analyte (R6G).

Hereafter, based on the obtained results, some suggestions for future work are to deposit ZnO *NRs* in different substrates (*e.g.* paper, where the NRs are tilted, allowing the laser to possibly activate more *hot spots*); study and optimization of obelisk nanorods coated with silver thin film with different thicknesses; optimization of microfluidics device design and to perform a study of limit detection, stability and reproducibility of the microfluidics device in terms of SERS applications.

References

1. Fasano, E., Cirillo, T., Esposito, F. & Lacorte, S. Migration of monomers and plasticizers from packed foods and heated microwave foods using QuEChERS sample preparation and gas chromatography/mass spectrometry. *LWT - Food Sci. Technol.* **64,** 1015–1021 (2015).
2. Hickert, S., Bergmann, M., Ersen, S., Cramer, B. & Humpf, H. U. Survey of Alternaria toxin contamination in food from the German market, using a rapid HPLC-MS/MS approach. *Mycotoxin Res.* **32,** 7–18 (2016).
3. Zheng, J. & He, L. Surface-Enhanced Raman Spectroscopy for the Chemical Analysis of Food. *Compr. Rev. Food Sci. Food Saf.* **13,** 317–328 (2014).
4. Schlücker, S. Surface-Enhanced Raman Spectroscopy : Concepts and Chemical Applications Angewandte. 4756–4795 (2014). doi:10.1002/anie.201205748
5. Siebert, F. & Hildebrandt, P. *Theory of Infrared Absorption and Raman Spectroscopy*. *Vibrational Spectroscopy in Life Science* (Wiley-VCH Verlag GmbG & Co. KGaA, 2008). doi:10.1002/9783527621347.ch2
6. Kleinman, S. L. *et al.* Structure Enhancement Factor Relationships in Single Gold Nanoantennas by Surface-Enhanced Raman Excitation Spectroscopy. *J. Am. Chem. Soc.* **135,** 301–308 (2013).
7. Wang, C. & Yu, C. Analytical characterization using surface-enhanced Raman scattering (SERS) and microfluidic sampling. *Nanotechnology* **26,** 92001 (2015).
8. Araújo, A. *et al.* Highly efficient nanoplasmonic SERS on cardboard packaging substrates. *Nanotechnology* **25,** 415202 (2014).
9. Schlücker, S. Surface-enhanced raman spectroscopy: Concepts and chemical applications. *Angew. Chemie - Int. Ed.* **53,** 4756–4795 (2014).
10. Le Ru, E. C. & Etchegoin, P. G. Rigorous justification of the |E|4 enhancement factor in Surface Enhanced Raman Spectroscopy. *Chem. Phys. Lett.* **423,** 63–66 (2006).
11. Valley, N., Greeneltch, N., Duyne, R. P. Van & Schatz, G. C. A Look at the Origin and Magnitude of the Chemical Contribution to the Enhancement Mechanism of Surface-Enhanced Raman Spectroscopy (SERS): Theory and Experiment. *Phys. Chem.* (2013). doi:10.1021/jz4012383
12. LeRu, E. C., Meyer, M., Etchegoin, P. G., Le Ru, E. C. & Blackie, E. Surface Enhanced Raman Scattering Enhancement Factors: A Comprehensive Study. *J. Phys. Chem. C* **111,** 13794–13803 (2007).
13. Sakano, T. *et al.* Surface enhanced Raman scattering properties using Au-coated ZnO nanorods grown by two-step, off-axis pulsed laser deposition. *J. Phys. D. Appl. Phys.* **41,** 235304 (2008).
14. Stiles, P. L., Dieringer, J. A., Shah, N. C. & Van Duyne, R. P. Surface-Enhanced

Raman Spectroscopy. *Annu. Rev. Anal. Chem.* **1,** 601–626 (2008).

15. Coluccio, M. L. *et al.* Silver-based surface enhanced Raman scattering (SERS) substrate fabrication using nanolithography and site selective electroless deposition. *Microelectron. Eng.* **86,** 1085–1088 (2009).
16. Khlebtsov, B. N., Khanadeev, V. A., Yu, M., Bagratashvili, V. N. & Khlebtsov, N. G. SERS Substrates Based on Self-Assembled PEGylated Gold and Gold – Silver Core – Shell Nanorods. (2013). doi:10.1021/jp408359p
17. Fales, A. M., Yuan, H. & Vo-Dinh, T. Development of hybrid silver-coated gold nanostars for nonaggregated surface-enhanced raman scattering. *J. Phys. Chem. C* **118,** 3708–3715 (2014).
18. Baca, A. J. *et al.* Molded plasmonic crystals for detecting and spatially imaging surface bound species by surface-enhanced Raman scattering. *Appl. Phys. Lett.* **94,** 100–102 (2009).
19. Halvorson, R. A. & Vikesland, P. J. Surface-enhanced Raman spectroscopy (SERS) for environmental analyses. *Environ. Sci. Technol.* **44,** 7749–7755 (2010).
20. Mohiddon, M. A., Sangani, L. D. V. & Krishna, M. G. Scanning near field optical microscopy of gold nano-disc arrays fabricated by electron beam lithography and their application as surface enhanced Raman scattering substrates. *Chem. Phys. Lett.* **588,** 160–166 (2013).
21. Mostafa, N. Y., Heiba, Z. K. & Ibrahim, M. M. Structure and optical properties of ZnO produced from microwave hydrothermal hydrolysis of tris(ethylenediamine)zinc nitrate complex. *J. Mol. Struct.* **1079,** 480–485 (2015).
22. Caglar, Y., Gorgun, K. & Aksoy, S. Effect of deposition parameters on the structural properties of ZnO nanopowders prepared by microwave-assisted hydrothermal synthesis. *Spectrochim. Acta - Part A Mol. Biomol. Spectrosc.* **138,** 617–622 (2015).
23. Pimentel, A. *et al.* Synthesis of long ZnO nanorods under microwave irradiation or conventional heating. *J. Phys. Chem. C* **118,** 14629–14639 (2014).
24. Li, A. *et al.* Direct electrodeposition of ZnO nanotube arrays in anodic alumina membranes. *J. Phys. Chem. C* **111,** 7288–7291 (2007).
25. Rodrigues, J. *et al.* Synthesis, structural and optical characterization of ZnO crystals grown in the presence of silver. *Thin Solid Films* **520,** 4717–4721 (2012).
26. Park, J. A., Moon, J., Lee, S. J., Lim, S. C. & Zyung, T. Fabrication and characterization of ZnO nanofibers by electrospinning. *Curr. Appl. Phys.* **9,** S210–S212 (2009).
27. Imran, M., Haider, S., Ahmad, K., Mahmood, A. & Al-masry, W. A. Fabrication and characterization of zinc oxide nanofibers for renewable energy applications. *Arab. J. Chem.* 1–6 (2013). doi:10.1016/j.arabjc.2013.01.013
28. Ma, X., Zhang, H., Ji, Y., Xu, J. & Yang, D. Sequential occurrence of ZnO nanopaticles, nanorods, and nanotips during hydrothermal process in a dilute aqueous solution. *Mater. Lett.* **59,** 3393–3397 (2005).

29. Pimentel, A. *et al.* Effect of solvents on ZnO nanostructures synthesized by solvothermal method assisted by microwave radiation: a photocatalytic study. *J. Mater. Sci.* **50,** 5777–5787 (2015).

30. Kim, D. *et al.* Microfluidic-SERS devices for one shot limit-of-detection. *Analyst* **139,** 3227–3234 (2014).

31. Liu, G. L. & Lee, L. P. Nanowell surface enhanced Raman scattering arrays fabricated by soft-lithography for label-free biomolecular detections in integrated microfluidics. *Appl. Phys. Lett.* **87,** (2005).

32. Pimentel, a *et al.* Microwave Synthesized ZnO Nanorods Arrays for UV Sensors : a Seed Layer Annealing Temperature Study. (2016). doi:10.3390/ma9040299

33. Schmidt-Mende, L. & MacManus-Driscoll, J. L. ZnO - nanostructures, defects, and devices. *Mater. Today* **10,** 40–48 (2007).

34. Kim, G. S., Ansari, S. G., Seo, H. K., Kim, Y. S. & Shin, H. S. Growth and morphological study of zinc oxide nanoneedles grown on the annealed titanate nanotubes using hydrothermal method. *J. Appl. Phys.* **102,** (2007).

35. Jensen, L. & Schatz, G. C. Resonance Raman Scattering of Rhodamine 6G as Calculated Using Time-Dependent Density Functional Theory. *Phys. Chem.* 5973–5977 (2006).

36. Polsongkram, D. *et al.* Effect of synthesis conditions on the growth of ZnO nanorods via hydrothermal method. *Phys. B Condens. Matter* **403,** 3713–3717 (2008).

37. Wood, A. *et al.* Size Effects in Zno: The Cluster to Quantum Dot Transition. *Aust. J. Chem.* **56,** 1051–1057 (2003).

38. Wahab, R. *et al.* Low temperature solution synthesis and characterization of ZnO nano-flowers. *Mater. Res. Bull.* **42,** 1640–1648 (2007).

39. Umar, A., Kim, S. H., Lee, Y. S., Nahm, K. S. & Hahn, Y. B. Catalyst-free large-quantity synthesis of ZnO nanorods by a vapor-solid growth mechanism: Structural and optical properties. *J. Cryst. Growth* **282,** 131–136 (2005).

40. Song, J. & Lim, S. Effect of Seed Layer on the Growth of ZnO Nanorods. *J. Phys. Chem. C* **111,** 596–600 (2007).

41. Tay, C. B., Chua, S. J. & Loh, K. P. Investigation of morphology and photoluminescence of hydrothermally grown ZnO nanorods on substrates pre-coated with ZnO nanoparticles. *J. Cryst. Growth* **311,** 1278–1284 (2009).

42. Liu, Y. & Gao, W. Growth process, crystal size and alignment of ZnO nanorods synthesized under neutral and acid conditions. *J. Alloys Compd.* **629,** 84–91 (2015).

43. Baruah, S. & Dutta, J. pH-dependent growth of zinc oxide nanorods. *J. Cryst. Growth* **311,** 2549–2554 (2009).

44. Li, Q. *et al.* Fabrication of ZnO nanorods and nanotubes in aqueous solutions. *Chem. Mater.* **17,** 1001–1006 (2005).

45. Ghayour, H., Rezaie, H. R., Mirdamadi, S. & Nourbakhsh, A. A. The effect of seed layer thickness on alignment and morphology of ZnO nanorods. *Vacuum* **86,** 101–105 (2011).

46. Ting, C. C. *et al.* Compact and vertically-aligned ZnO nanorod thin films by the low-temperature solution method. *Thin Solid Films* **518,** 4156–4162 (2010).

47. İkizler, B. & Peker, S. M. Effect of the seed layer thickness on the stability of ZnO nanorod arrays. *Thin Solid Films* **558,** 149–159 (2014).

48. Kelly, K. L., Coronado, E., Zhao, L. L. & Schatz, G. C. The Optical Properties of Metal Nanoparticles: The Influence of Size, Shape, and Dielectric Environment. *J. Phys. Chem. B* **107,** 668–677 (2003).

49. Attanayake, T., Premaratne, M. & Agrawal, G. P. Characterizing the Optical Response of Symmetric Hemispherical Nano-dimers. *Plasmonics* **10,** 1453–1466 (2015).

50. Nakayama, K., Tanabe, K. & Atwater, H. A. Plasmonic nanoparticle enhanced light absorption in GaAs solar cells. *Appl. Phys. Lett.* **93,** 5–8 (2008).

51. Smith, W. E. Practical understanding and use of surface enhanced Raman scattering/surface enhanced resonance Raman scattering in chemical and biological analysis. *Chem. Soc. Rev.* **37,** 955–964 (2008).

52. Tang, H. *et al.* Arrays of cone-shaped ZnO nanorods decorated with ag nanoparticles as 3D surface-enhanced raman scattering substrates for rapid detection of trace polychlorinated biphenyls. *Adv. Funct. Mater.* **22,** 218–224 (2012).

53. McLellan, J. M., Li, Z. Y., Siekkinen, A. R. & Xia, Y. The SERS activity of a supported ag nanocube strongly depends on its orientation relative to laser polarization. *Nano Lett.* **7,** 1013–1017 (2007).

54. Jurablu, S., Farahmandjou, M. & Firoozabadi, T. P. Multiple-layered structure of obelisk-shaped crystalline nano-ZnO prepared by sol–gel route. *J. Theor. Appl. Phys.* **9,** 261–266 (2015).

55. Yasui, T. *et al.* Confocal microscopic evaluation of mixing performance for three-dimensional microfluidic mixer. *Anal. Sci.* **28,** 57–9 (2012).

5 Attachments

Attachment A

Table of laser parameters for etching the PDMS.

Table 5. 1 - Laser parameters for Microfluidics device pattern

Drawn diameter (mm)	*Laser Power (%)*	*Velocity (%)*	*Thickness drawn (mm)*
1	90	60	100

Attachment B

Table with variation of ZnO nanorods with different time and temperature synthesis.

Table 5. 2 - Diameter and length variation of ZnO NRs at different temperatures and synthesis time constant (15 min) and ZnO NRs diameter and length variation at 100ºC using different times of synthesis.

		Time (min)					*Temperature (ºC)*			
		5	15	30	45		70	100	130	150
100ºC	Diameter (nm)	45.6	56.3	68.2	153.3	15 min	54.1	56.3	58.4	57.2
	Length (nm)	163.4	353.5	357.1	360.4		173.4	353.5	372.2	378.2

Attachment C

XRD of ZnO seed layer thickness: 100, 150, 200 and 300 nm.

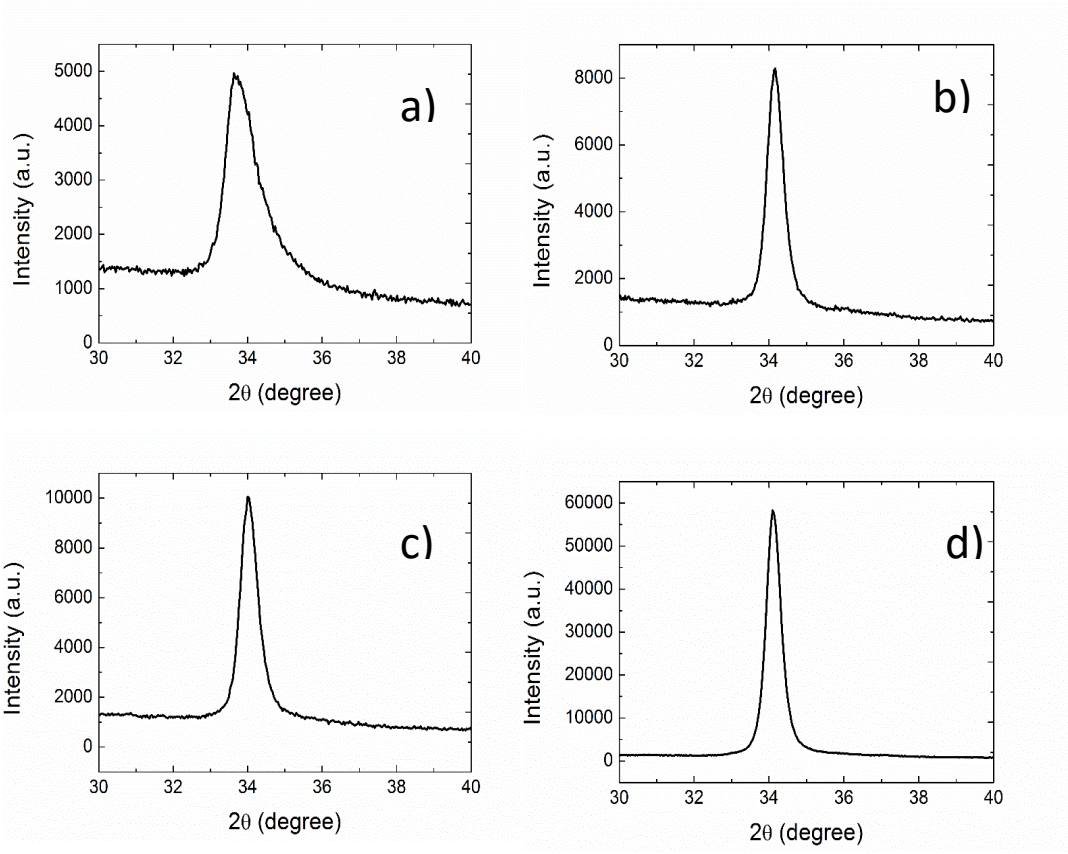

Figure 5. 1 - XRD of ZnO seed layer thickness: a) 100 nm; b) 150 nm; c) 200 nm; d) 300 nm.

Attachment D

Average enhancement factor values, calculated for 1360 and 1509 cm^{-1} bands.

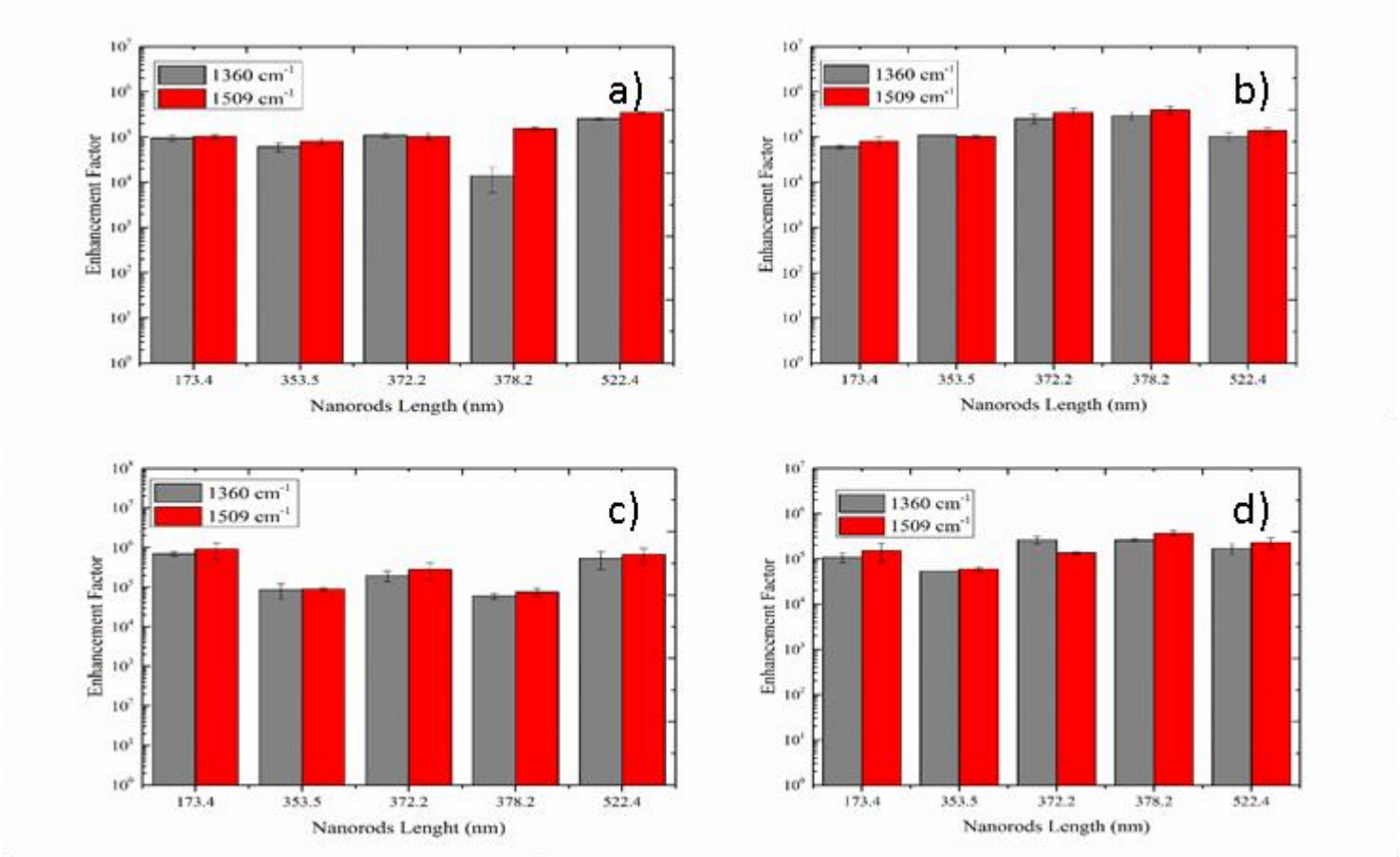

Figure 5. 2 - Average EF values calculated using the vibrational bands areas at 1360 and 1509 cm-1 for: a) 2 nm Ag NPs; b) 4 nm Ag NPs; c) 6 nm Ag NPs; d) 8 nm Ag NPs.

Attachment E

Average enhancement factor value for ZnO NRs with the same length, using different Ag thickness.

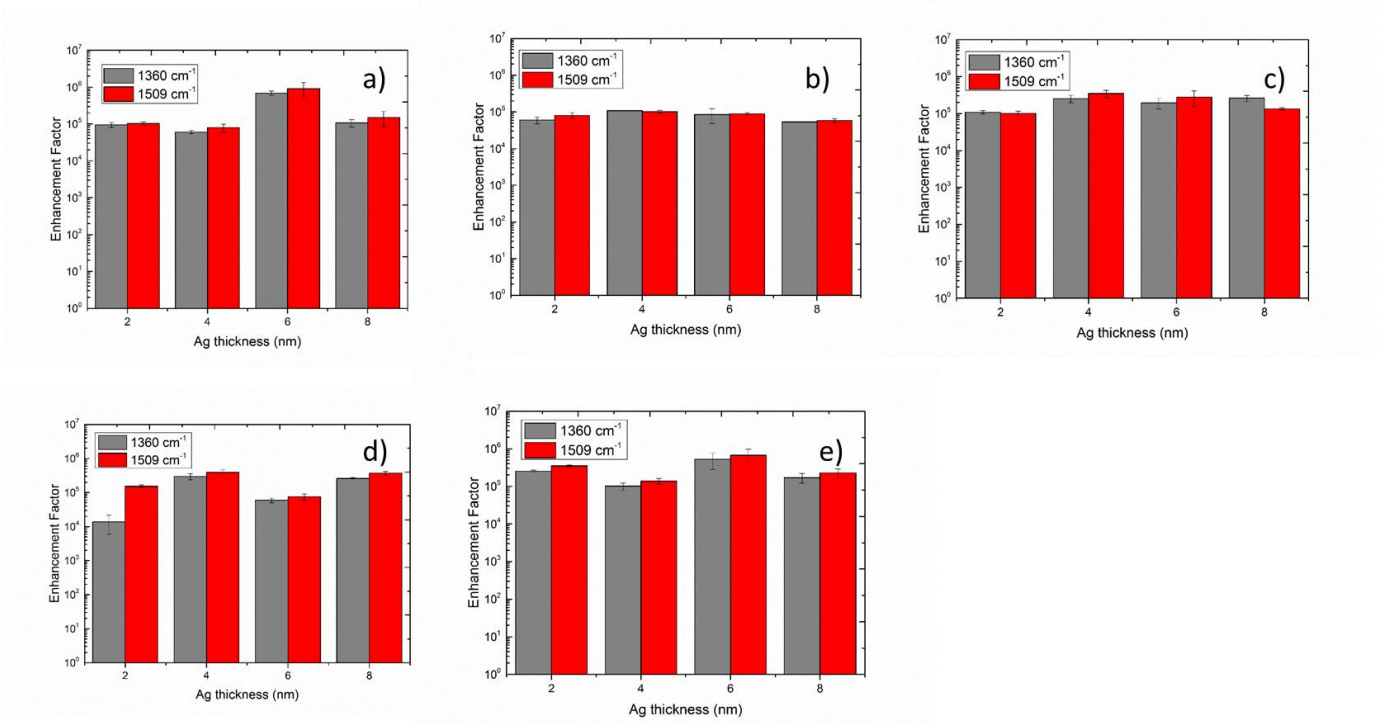

Figure 5. 3 - Average EF values of different Ag thickness with NRs length: a) 173 nm; b) 353 nm; c) 362 nm; d) 372 nm; e) 522 nm.